HAL
open science

Effects of Testing Parameters on the Susceptibility to Hydrogen Embrittlement in Precipitation-Hardened Nickel-Based Alloys : the Role of Continuous Straining

D.F. Martelo, Rd Panji Maulana, R. Leiva-Garcia, G.R. Joshi, R. Morana, R. Akid

To cite this version:

D.F. Martelo, Rd Panji Maulana, R. Leiva-Garcia, G.R. Joshi, R. Morana, et al.. Effects of Testing Parameters on the Susceptibility to Hydrogen Embrittlement in Precipitation-Hardened Nickel-Based Alloys : the Role of Continuous Straining. Corrosion Science, 2022, 199, pp.110171. 10.1016/j.corsci.2022.110171 . hal-03655101

HAL Id: hal-03655101
https://ifp.hal.science/hal-03655101v1

Submitted on 29 Apr 2022

HAL is a multi-disciplinary open access archive for the deposit and dissemination of scientific research documents, whether they are published or not. The documents may come from teaching and research institutions in France or abroad, or from public or private research centers.

L'archive ouverte pluridisciplinaire **HAL**, est destinée au dépôt et à la diffusion de documents scientifiques de niveau recherche, publiés ou non, émanant des établissements d'enseignement et de recherche français ou étrangers, des laboratoires publics ou privés.

Effects of testing parameters on the susceptibility to hydrogen embrittlement in precipitation-hardened nickel-based alloys: the role of continuous straining

D.F. Martelo[a], Rd Panji Maulana[a], R. Leiva-garcia[a], G.R. Joshi[b], R. Morana[c] and R. Akid[a]

[a] BP International Centre for Advanced Materials, School of Materials, University of Manchester, M13 9PL, UK

[b]IFP Energies Nouvelles, Rond-point de l'échangeur de Solaize, 69630, Solaize, France

[c] BP Exploration Operating Company Limited, Chertsey Road, Sunbury-on-Thames, TW16 7LN, UK

Abstract

The hydrogen embrittlement susceptibility of two precipitation hardened nickel-based alloys was studied. Conventional slow strain rate testing results are compared against data obtained from a modified Rising Step Loading Test with interrupted hydrogen charging to determine the role of defects in the passive layer caused by local straining. The results obtained in these tests, show that the elongation to failure for most cases was independent of the testing methodology. XPS and EIS studies indicate changes to the passive film structure caused by CP. These results imply that during hydrogen charging, the passive film is partially dissolved facilitating hydrogen uptake.

1. Introduction

UNS N07716 (625+) and UNS N7718 (718) nickel based alloys are used in the oil and gas (O&G) sector due to the beneficial combination of high corrosion resistance and high mechanical strength [1]. In particular, 625+ is used when the environmental conditions are expected to be very aggressive, i.e. 625+ has higher critical pitting potential than 718. These alloys are strengthened by the precipitation of γ`` (Ni_3Nb) and γ` ($Ni_3(Al,Ti)$) particles in the Ni matrix. Amongst these, the γ'' precipitate has the larger volume fraction in both alloys due to the higher alloying content of Nb [2-3]. During their commissioning stage in O&G applications, these so-called precipitation hardened (PH) nickel based alloys are exposed to hydrogen uptake scenarios, e.g. during electroplating or chemical combination of cleaning doping products [1], or through specific well design where the nickel based components can be connected to an external cathodic protection system [4-6]. Exposure to these conditions has the potential to result in catastrophic hydrogen induced brittle failures [1,7].

For alloy 718 in an aged heat treatment condition, Zhang et al. [8] used high resolution electron microscopy to propose that during the SSRT of cathodically pre-charged specimens, at 7.7mA/cm^2 for 7 days in a 1M NaCl solution, the failure of the specimens was caused by the nucleation of nano-voids at the intersection of Dislocation Slip Bands (DSBs) and subsequent cracking along the {111} plane due to slip localization. This mechanism of fracture is consistent with observations obtained from other relevant hydrogen embrittlement (HE) studies under diverse testing conditions [9-17]. Such studies reveal that the morphology of fracture changes with H content within the alloy [14-16] and arguably with other

parameters i.e. loading rate [9] and microstructure [10-11]. The effect of H content on the morphology of fracture has been observed in other PH nickel-based alloys [18]. Most of the data acquired for 718 propose that its HE susceptibility scales with an increase in the cathodic potential [14, 16-17]. However, during crack propagation tests conducted by Lillard *et al* in samples of a heat treatment condition that were defined as Sub-STA (Solution anneal at 954°C and aged at 718°C for 8 hours), the threshold stress intensity factor under environmental conditions (K_{th-E}) reached a minimum value at intermediate cathodic potentials. These results suggest that embrittlement may be better correlated with other relevant parameters i.e. the concentration of diffusible H concentration at the crack tip [18].

With respect to 625+, this alloy in has, in general, shown a higher susceptibility to HE than 718 [17, 19-20], which has been related to the grain boundary precipitation [17]. However, this is not a simple relationship. For example, there are different types of grain boundary precipitate in 625+, and the contribution of each of these to the fracture process seems to be different [21]. Furthermore, grain boundary engineering developments have shown that the crack propagation mode in 625+ can be shifted from intergranular to transgranular producing an increase in the stress intensity factor threshold (K_t) during Rising Step Loading Tests (RSLT) [22]. In both studies, the interactions of hydrogen and dislocation movement play a major role in hydrogen embrittlement.

Independent of the HE mechanism, H entry is the first step of the hydrogen embrittlement (HE) process [23]; the efficiency of H entry depends on the severity of the hydrogenating environment, the hydrogen activity at the material interface, and the nature of the surface [24]. For example, it has been observed that the chromium oxide layer of a stainless steel has the capacity to inhibit or delay the absorption of H into the material bulk [25]. This is suggested to be down to an enhanced H uptake at the bare metal (against the passive oxide film), rather than lower diffusion across the passive oxide *per se* [24]. For some corrosion-assisted cracking processes, material degradation appears to be enhanced by passive film rupture during straining. For example, in the case of low alloy steel corrosion in high temperature water [26], it has been established that component straining is a key precursor to corrosion assisted crack growth. This is suggested to be due to the destruction of the brittle mixed oxide surface film, during active straining, compared to observations from static tests. In a similar context, Liu et al. [27] suggested that intergranular stress corrosion cracking in austenitic stainless steels in high temperature water involves the fracture of the passive oxide at the crack tip through tensile or shear strains. Nonetheless, we feel that direct evidence of this oxide rupture hypothesis is somewhat lacking in the literature. For duplex stainless steels, Griffith et al. [28] show no direct correlation between H transport properties (in the bulk-measured at pristine surfaces) and the elongation to failure measured during SSRT with *in situ* H charging, and suggest that H uptake through ruptured passive film sites could be a significant factor.

In the case of nickel-based alloys, data obtained from the literature suggest that local H uptake through film rupture as well as bulk H uptake are both relevant considerations. **Figure 1** shows the elongations to failure of SSRTs in pre-charged specimens and during *in situ* H

charging in 1M NaCl and 0.5M H_2SO_4. The pre-charged tests may be categorized as a test in which bulk H uptake is important, whereas both bulk H uptake and enhanced H uptake through film rupture must be prevalent during tensile tests with continuous *in situ* H-charging. The blue arrows in **Figure 1** point in the direction going from pre-charged SSRT results (hollow symbols) to *in situ* H charging SSRT results (filled symbols).

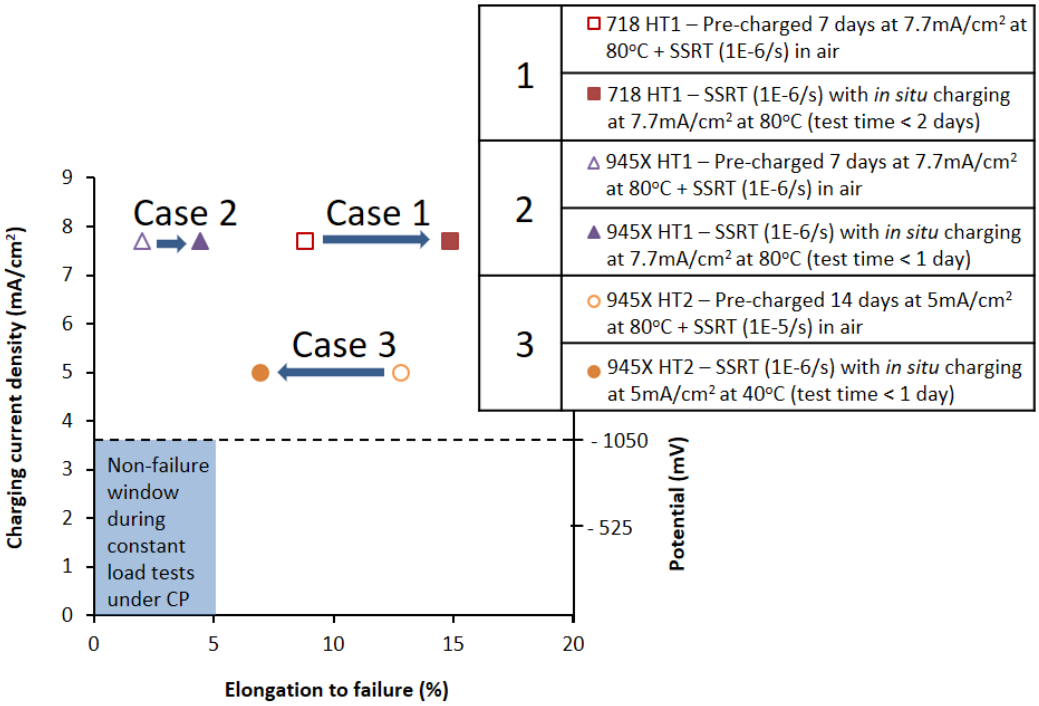

Figure 1. Elongation to failure *vs.* hydrogen charging in PH Ni-based alloys 718 and 945X as a function of the H entry protocol (Bulk H uptake/pre-charge vs. local H uptake/ *in situ* charging). Case 1 and 2 data are taken from Sampath et al. [12, 29], while Case 3 was taken from McCoy et al. [30]; The non-failure windows were constructed using data taken from G. Stenerud [31].

Considering that the elongation to failure in cases 1 and 2 are higher during *in situ* charging with respect to hydrogen pre-charging, it appears that bulk H uptake has a more significant impact on the embrittlement behaviour of these alloys in the studied conditions. Conversely, in case 3, 945X (HT2) suffers a significant loss in for the *in situ* H-charging scenario indicating that local H uptake (during passive film rupture) is likely relevant. It should be recognised that pre-charging for all cases is conducted on unstressed samples using "unrealistic"[1], high charging current densities. In addition, for case 3, the strain rate in the pre-charged specimen was increased (to 1×10^{-5} s^{-1}) compared to the test conducted in the *in situ* H charged specimen (1×10^{-6} s^{-1}). Note: due to dislocation assisted Hydrogen diffusion, the choice of strain rate during a SSRT should be considered. The 'non-failure' window in

[1] Such values of charging current density are not expected during real-world cathodic protection (CP) conditions

Figure 1 is created from constant load tests[2] data, where no cracking is observed. Other results in the literature suggest that H charging during dynamic straining is not the only parameter to consider in order to assess the HE susceptibility of nickel based alloys; the dynamic strain rate is also to be afforded importance [32].

In situ SSRT results are informative and relevant because the simultaneous continuous straining and cathodic charging "replicate" observed service conditions such as start-ups, load-ramps and shutdowns [26], when failures are possible. Nonetheless, this methodology has its drawbacks [33]. For example, extensive plastic deformation beyond that expected in service is imposed, and it does not provide design information (i.e. the fracture stress obtained from SSRT under cathodic protection (CP) depends on the strain rate and the specimen size amongst other factors). A detailed study of the significance and development of the SSRT method can be found in reference [33].

A major inconvenience of *in situ* H-charging SSRT of Corrosion Resistant Alloys (CRAs) is that dynamic straining may severely rupture the passive layer. Thus, for instance, the mechanical performance between two different alloy variants is difficult to distinguish since passive layer properties and their rupture dominate the cracking response. For example, the passive layer of 625+ is significantly more stable than the passive layer of 718 due to the higher alloying content of Cr and Mo in the former PH alloy. Thus, the results presented in this article are a part of a broader research programme that seeks to establish the dominant parameters during the assessment of the HE susceptibility of PH nickel based alloys, including continuous straining, the strain rate and the charging current density. To this end, to support classic environmental sensitive cracking tests, we have also used electrochemical impedance spectroscopy (EIS) (to assess the interfacial response during cathodic charging) and *ex situ* X-ray Photoelectron Spectroscopy (XPS) before and after cathodic charging (in an effort to evaluate the changes in top-surface (passive layer) evolution of the Ni-base alloys) used in this research. In this study, tests were conducted using a modified RSLT methodology in comparison to SSRT to determine if continuous straining during SSRT enhances H uptake and increases the perceived susceptibility to HE.

2. Experimental procedure

2.1. Materials

Ni-base alloys 718 and 625+ were used in this research. The chemical composition of both alloys is given in **Table 1**. For all work, samples were studied in the aged condition corresponding to the following heat treatments according to API standard 6A718: Alloy 718

[2] The non-failure condition window was established using tests at constant load during 30 days of *in situ*-charging in an aged hardened nickel alloy 718 in a solution of 3.5 wt% NaCl at an applied voltage of -1.05V vs silver/silver chloride electrode at room temperature; the samples were pre-charged previous to the tests at 120°C. For the non-failure condition window exposed in Figure 1, the strain and charging current density were extrapolated from the stress strain curve reported in the work of G. Stenerud [31] and from in-house potentiodynamic polarization curves.

was solution annealed at 1040°C for 1h and aged at 760°C for 7 hours, whereas Alloy 625+ was solution annealed at 1040°C for 1h and double aged at 746°C for 5 hours and at 621°C for 12 hours. 625+ is designed with the intention of producing an alloy with high corrosion resistance and high strength. Thus, it comprises higher levels of Chromium and Molybdenum than 718 [34]. Some needles of δ phase (orthorhombic Ni_3Nb) can be observed decorating the grain boundary of 718, see inset in **Figure 2(a)** while Cr and Mo precipitates can be seen at the grain boundary of 625+, see inset in **Figure 2(b)**.

Table 1. Chemical Composition (wt. %)

Alloy	Ni	Cr	Nb	Mo	Ti	Al	C	Cu	Si	S	P	Fe
718	54.7	18.6	5.07	3.04	0.88	0.45	0.018	0.06	0.10	0.0002	0.009	Bal
625+	61.1	21	3.65	8.1	1,49	0.22	0.015	0.05	0.16	0.0002	0.011	Bal

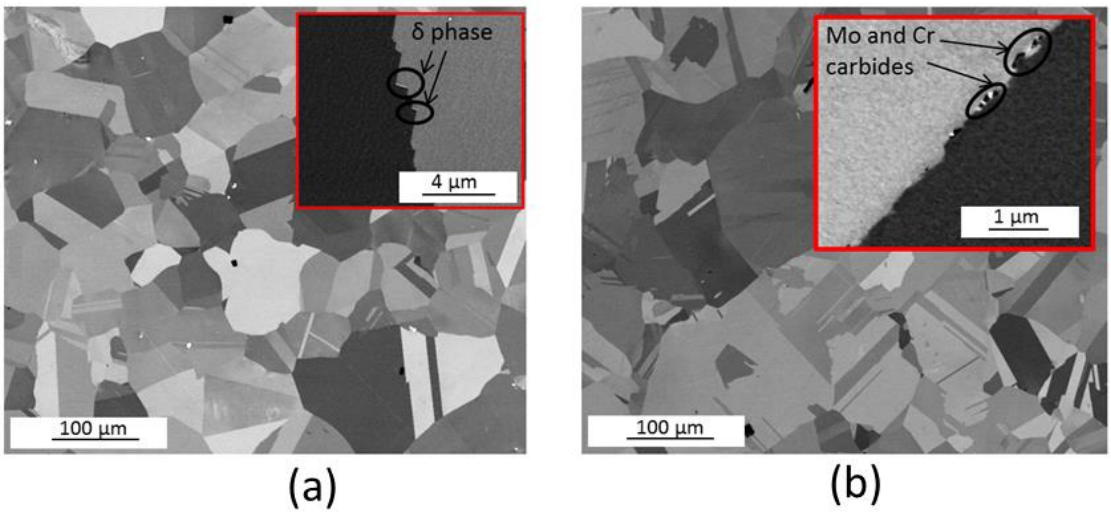

Figure 2. SEM images of the microstructure of alloys (a) 718, showing an inset image of some δ phase needles and (b) 625+, showing an inset image of the Cr and Mo carbides at the grain boundary.

2.2. Sample preparation

For mechanical tests, sample blanks were extracted from the ingot by electrical discharge machining (EDM), and subsequently solution annealed at 1040°C for 1 hour and air cooled. In this condition, the blanks were machined into tensile specimens following the specifications from NACE TM0198 (subsize specimens) [35]. Following the machining/ageing heat treatment, the samples were electro-polished using a procedure defined in Reference [20]. Tensile test sample surfaces were ground using 1200 grit SiC paper parallel to the loading axis prior to starting mechanical tests.

Samples used for Electrochemical Impedance Spectroscopy (EIS) and X-ray Photoelectron Spectroscopy (XPS) analyses were obtained from the same ingot as the tensile specimens. For the EIS tests, the samples were spot welded to a conducting CuSn wire and mounted in cold-setting epoxy resin. After curing of the resin, the samples were ground sequentially with SiC paper from grit 320 to grit 1200 and exposed a final surface area of approximately 1 cm^2. A lacquer was applied to the spot weld/sample joint and on the sample's edges to avoid galvanic and crevice corrosion respectively during immersion testing.

2.3. Mechanical testing

HE susceptibility of these alloys has been investigated using two different methodologies:

Slow Strain Rate Test (SSRT): This method involves the application of a slow strain rate (10^{-6} s^{-1}) during which the tensile specimen is subjected to galvanostatic cathodic polarization (the source of absorbed atomic hydrogen) at 5 mA cm^{-2} in a solution of 0.5 mol dm^{-3} H_2SO_4. This methodology is currently used in the O&G sector during materials selection, to discern if a Precipitation Hardened (PH) nickel base alloy is susceptible to HE. We have used a test temperature of 40°C, and full details of this experimental procedure can be found in Reference [36].

Rising Step Loading Test (RSLT) with interrupted charging: This method was devised to investigate differences in HE susceptibility that might result from H uptake through the passive film / defects in the passive film (local H uptake) caused by dynamic straining during *in situ* charging SSRT. This protocol is based on the hypothesis that H entry should be easier on fresh or "active" metal surfaces (localised regions devoid of passive film coverage) [37]. In this methodology, H is only introduced into the metal at constant displacement via galvanostatic cathodic polarization; during the rising step[3], which involves increasing the load at a strain rate of 10^{-4} s^{-1} ,the specimen is allowed to remain at its open circuit potential (OCP). The subsequent period spent under galvanostatic cathodic charging at constant load is determined using the elongation to failure from SSRT as a reference at its corresponding charging current density. This criterion is adopted to ensure that the charging time at any given strain is identical (within the range of the step times) in every methodology. RSLT employed identical environmental conditions as used in the TOTAL method [36] at two cathodic current densities of 5 mA cm^{-2} and 0.6 mA cm^{-2}. Before and after every loading step, the sample remained at OCP for 5 minutes. A schematic illustration of the load versus time profile for an RSLT is provided in **Figure 3**.

[3] This strain rate was used to expedite the loading step to avoid significantly altering the test duration; these SSRT and RSLT with interrupted charging test durations should be the same to dismiss the possible influence of H diffusion into the metal. The new strain rate should play no bearing on the result since nickel-base alloys are still very susceptible at this strain rate as shown in Demetriou et al. [11].

In both SSRT and RSLT methodologies, the susceptibility to HE is measured using the time to failure; samples with longer times to failure may be considered less susceptible to HE[4]. A large difference in the time to failure between the SSRT with respect to its corresponding RSLT indicates the possible effects of local H uptake through defects in the passive film.

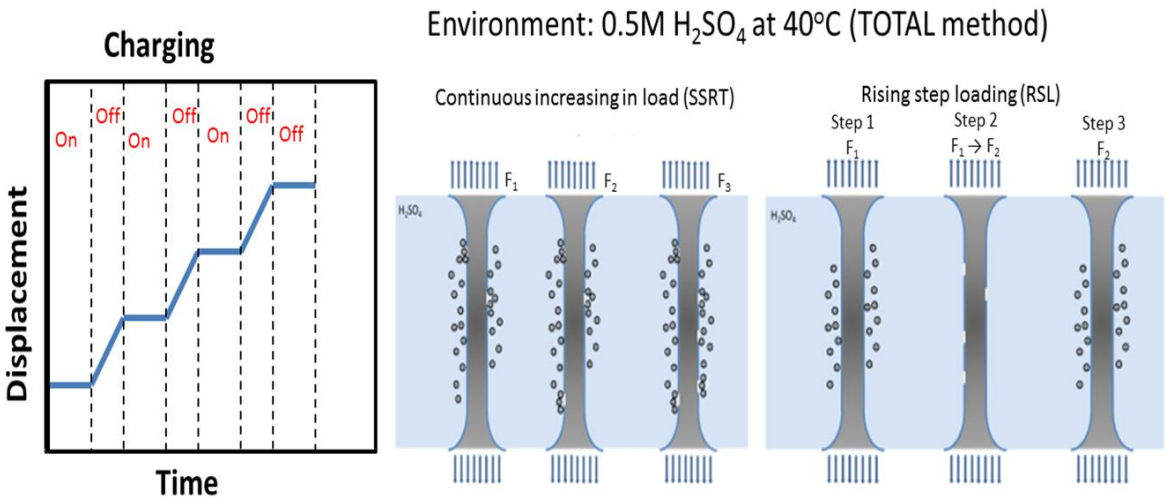

Figure 3. Schematic of the RSLT protocol; "on" implies cathodic polarisation, while "off" denotes zero current (the sample is at OCP). Specimens are kept at constant displacement during charging; note, the specimen is displaced at a strain rate of 1 x 10^{-4} s^{-1} during the rising step. In the figure, F corresponds to the applied force.

2.4. EIS measurements

Potentiostatic EIS tests were conducted in an electrochemical cell placed within a nitrogen glovebox to minimize the interaction of the surface of the specimens with atmospheric oxygen. The samples were H charged in a solution of 0.5 M H_2SO_4 at room temperature using the same electrochemical conditions of the slow strain rate tests following the cycle of measurements illustrated in **Figure 4**. At times before and after this cathodic polarisation, EIS measurements were carried out on the samples in N_2-deaerated solution of 1 g/L NaCl (0.017M, pH = 7.0). This solution was chosen as it serves as a favourable, neutral 'reference' electrolyte for probing any changes to the interfacial impedance.

[4] The time to failure was used as a criterion to measure the susceptibility to HE in this research due to similarities in the elongation to failure between both materials in test in inert environment of 30.41% for 718 and 34.34% for 625+. Since SSRTs are conducted at constant strain rate, the time to failure is proportional to the elongation to failure.

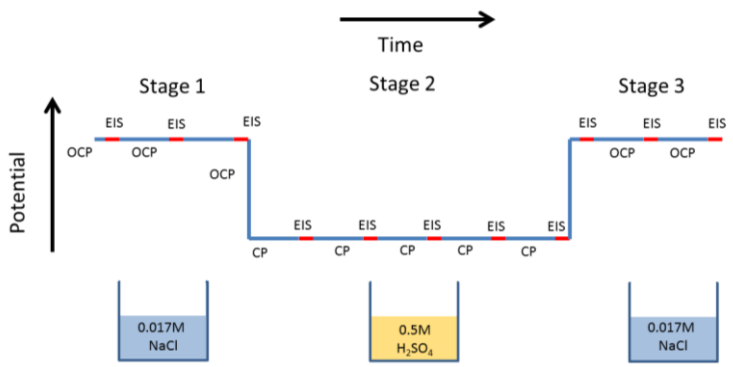

Figure 4. Protocol used for conducting electrochemical impedance spectroscopy to measure the possible degradation of the passive layer. OCP: measurement of Open Circuit Potential (OCP) data. EIS: measurements of Electrochemical Impedance Spectroscopy (EIS) data.

The first EIS measurement (9 kHz to 90 mHz, AC cycle (rms) = 7.07mV) was taken under OCP after 3 minutes immersion and at subsequent intervals of: 10, 20, 30, 80, 120 minutes for a period lasting 3 hours. This period serves as a time for the passive layer to hydrate and equilibrate in the aqueous medium. In the second stage, still within the glove box, the Ni-base alloy working electrodes were transferred to a solution of (deaerated) 0.5M H_2SO_4 (pH = 0) for a period of 12 hours under cathodic protection (CP) at either 5mA/cm^2 or 0.6mA/cm^2. EIS measurements were taken every hour ± 7.07 mV rms around the potential that matched the galvanostatic polarisation e.g. for 5mA/cm^2, a value of -550 mV_{OCP} was the fixed DC potential instead of the 'new' OCP. Finally, in stage 3, the samples are returned to the same solution of 1 g/L NaCl (0.017M, pH = 7.0) as stage 1, and EIS measurements around OCP are continued after 3 minutes immersion. Between each transfer, the samples were rinsed with deaerated, deionized water.

2.5. X-ray photoelectron spectroscopy (XPS)

A Kratos Axis Ultra Hybrid with a monochromatic Al Kα X ray source (1486.6 eV) instrument was used for XPS. A Pass Energy of 20eV was used for a survey spectrum of the samples in each condition and 80eV for the high resolution scans of: Cu 2p, Ni 2p, Fe 2p, Cr 2p, O 1s, C 1s, Mo 3d, Nb 3d and S 2p. The operating pressure of the analysis chamber was ≈ 5x10^{-7} Pa. A normal photoelectron emission angle was used during the scans (0°). Binding energies (BEs) were calibrated against the C1s carbon peak for each sample.

As in the case of the SSRT and EIS tests, the XPS measurements were conducted on specimen surfaces that had been charged at the two distinct cathodic current densities: 0.6mA cm^{-2} and 5mA cm^{-2} in a solution of 0.5 M H_2SO_4 at room temperature. The H charging period was 12 hours. In practical terms, inert atmosphere (N_2-purged) glove boxes were used in this setup. One of these was used to cathodically charge the Ni-base alloy specimen, and the other employed to transfer the samples into the XPS holder [38]. A vacuum tube apparatus was employed to transfer the specimens from the H charging glove box to the glove box placed in the XPS load-lock. More details about the test rig can be found in reference [39].

2.6. H concentration measurements

The H concentration was measured using an ELTRA OH 900. In this device, the hydrogen is extracted by melting small specimens inside a graphite crucible. The hydrogen content is detected using a thermal conductivity cell, and for quantification purposes, the machine is calibrated against Nickel standards prior to its use. The H concentration measurements were obtained from samples sectioned from the gauge length of the specimen submitted to CP adjacent to (but not including) the fracture surface, since the objective was to measure the H concentration related to the passive film breakdown that results from straining. In most cases, the H concentration measurements were taken in the two hours after the test termination. If a test finished overnight, the H concentration measurements were taken early in the morning of the next day.

2.7. Microscopy

SEM imaging was carried out to examine the microstructure and the fracture surfaces. In particular, the micrographs presented in this paper were taken using the backscatter detector of a FEI Magellan 400 XHR SEM at an accelerating voltage of 5kV. For the fracture surface analysis, a Zeiss EVO 50 SEM was used. The fracture surfaces were obtained after cutting the sections of the gauge length used for the H concentration measurements. To remove the cutting fluid from the fracture surface, the samples were cleaned in a solution of acetone and using an organic fibre brush. Subsequently, the samples were attached to a SEM stub using double-sided conductive carbon tape.

3. Results and Discussion

3.1. Mechanical tests

718

Figure 5(a) shows stress vs. time profiles for specimens of alloy 718 using conventional SSRT and the modified RSLT methodology. The results show that the time to failure increases (i.e. the susceptibility to HE decreases) with a decrease in applied cathodic current density. At high current densities (5 mA/cm^2), alloy 718 exhibits similar time to failure in RSLT and SSRT (black lines), although slightly lower elongation failure in the RSLT, **Table 2**. This was due to failure commencing at the beginning of the increase in elongation (stress) step. At lower charging current density (0.6 mA/cm^2), the elongation/time to failure is considerably greater in the RSLT (67h of *in situ* charging, red line) than under SSRT (41.5h of *in situ* charging, black line) at the same current density. Such a difference between the RSLT and SSRT at low current densities may imply that the contribution of local H uptake could be more significant compared to its relevance at high current densities[5].

[5] A table is presented in the supplementary material showing the standard deviation of SSRTs in Nickel alloys using similar environmental conditions used in this study. This data shows the scatter in the elongation to failure in these types of test.

Table 2. Time to failure, elongation to failure and elongation to failure ratio for the SSR and the RSL tests.

	718 SSRT 0.6 mA/cm^2	718 RSLT 0.6 mA/cm^2	718 SSRT 5 mA/cm^2	718 RSLT 5 mA/cm^2	625+ SSRT 0.6 mA/cm^2	625+ RSLT 0.6 mA/cm^2	625+ SSRT 5 mA/cm^2	625+ RSLT 5 mA/cm^2
Time to failure (h)	41.5	66.99	23.8	23.4	15.7	19.4	27.09	29.1
Elongation to failure (%)	14.96	25.33	8.5	5.1	5.6	8	9.7	8.1
Elongation to failure ratio	0.49	0.83	0.28	0.17	0.16	0.23	0.28	0.24

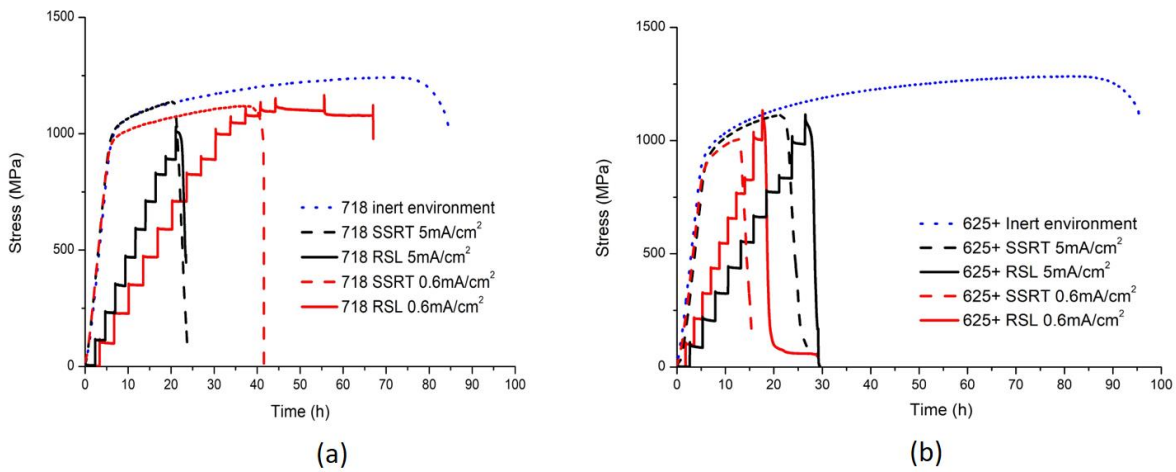

Figure 5: Stress-time curves from SSRT (smooth) and RSLT (zigzag) data for (a) alloy AR 718 and (b) 625+ in both the inert and H environments used in the TOTAL method at 5 mA/cm^2 and 0.6 mA/cm^2.

625+

In **Figure 5 (b)**; for alloy 625+, we note that the SSRT elongation/time to failure is smaller at 0.6 mA cm^{-2} compared to 5 mA cm^{-2}. This same trend holds for the RSLT results. Remarkably, the susceptibility to HE appears higher at the lower current density for this alloy. This curious finding is further probed with the support of data presented in the following sections.

The time to failure was always greater from the RSLTs for the same charging current density. However, this trend is not reflected in the elongation to failure data at 5mA/cm^2, where the higher elongation to failure is a consequence of the lower strain rate. This, in turn, allows the remaining ligament to sustain the load for longer leading to a higher extension value, see complementary **Figure A.2.** Comparing both alloys, the results indicate that 718 is less susceptible to HE, a difference that is more notable at 0.6 mA/cm^2.

3.2. XPS results

Most of the elements listed in the chemical composition of the Ni base alloys (**Table 1**) were found in the XPS wide scan spectra, with Cr and Ni being the most significant, after accounting for responses from C and O. **Table 3** lists the ratio of different elements against Ni obtained from the chemical analysis of the bulk material, and from the survey spectrum from the surface using XPS. The ratio is noted to increase for Cr, Nb and Mo, which suggests that all these elements are present in the passive layer of both alloys. Based on the shape and position of the peaks, with respect to the binding energies (BEs), the spectra confirm the presence of chromium oxides [40], molybdenum oxides [41-43] and niobium oxides [41,44] in the passive film of the reference sample. **Figure 6** shows the spectra obtained from Alloy 718, and **Figure 7** the spectra from 625+. The presence of Fe-oxyhydroxide compounds within the passive films could not be confirmed due to a strong Ni LMM auger peak masking the relevant spectral region. Fe, Cr and Mo are registered as the predominant elements present in the passive films of alloys with high Molybdenum content [45]. A small peak can be observed next to the Ni $2p_{3/2}$ metal peak in the high resolution energy spectra of nickel **Figure 6(a)** and **7(a)**, which could either be assigned to NiO [41] or $Ni(OH)_2$ [46] or both.

Table 3. Elemental analysis of alloys 718 and 625+ in the bulk and on the surface both normalized against the Ni content in the bulk and on the surface, respectively.

Alloy	Position	Ni/Ni	Cr/Ni	Nb/Ni	Mo/Ni
718	Bulk	1	0.34	0.104	0.055
	Surface	1	0.90	0.198	0.08
625+	Bulk	1	0.34	0.059	0.13
	Surface	1	1.33	0.114	0.28

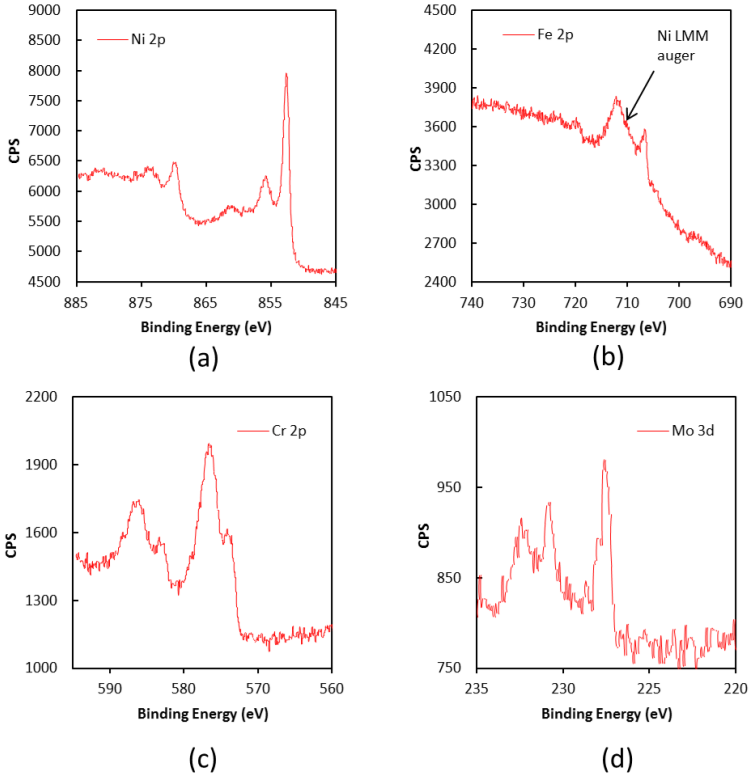

Figure 6. High resolution XPS spectra taken from the surface of Alloy 718 with a passive film formed in air for (a) Ni 2p, (b) Fe 2p, (c) Cr 2p and (d) Mo 3d.

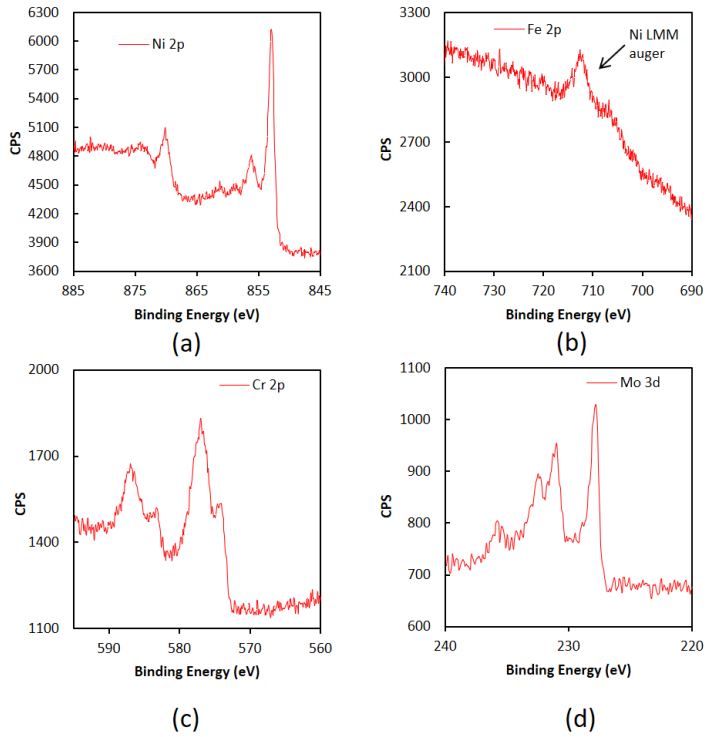

Figure 7. High resolution XPS spectra taken from the surface of Alloy 625+ with a passive film formed in air for (a) Ni 2p, (b) Fe 2p, (c) Cr 2p and (d) Mo 3d.

The passive film in Ni-based alloys is considered to be a bilayer, composed of an outer hydroxide/oxide film and an inner pristine oxide [41,47]. Conventionally, the chromium oxide in the inner layer is highlighted as the phase responsible for the corrosion resistance of Ni-Cr alloys [48]. On this basis, our interpretations of the evolution of the passive layer resulting from cathodic charging in 0.5M H_2SO_4 will be based on the high-resolution energy spectra of chromium. **Figure 8** shows the evolution of the chromium peaks, from the air formed films, with **Figure 8(a)** focusing on 718 and **Figure 8(d)** on Alloy 625+. For both alloys, after cathodic charging, **Figure 8(a-b)** for 718 and **Figure 8(d-e)** for 625+, the $2p_{3/2}$ (BE = 578.9 eV) and $2p_{1/2}$ (BE = 586.9eV) peaks corresponding to a Cr oxide decreased in size, whereas Cr metal peaks $2p_{3/2}$ and $2p_{1/2}$ increase (only the $2p_{3/2}$ peaks are highlighted in **Figure 8**. In **Table 4,** we find the ratio of Cr oxide: Cr metal. For this analysis, the peaks were fitted using a Shirley background with an asymmetric peak function in CasaXPS software with the following parameters LA(1.3,4,5) [49] for the Cr metal peak: - the Cr oxide peak was fitted using multiple peak fitting with a Gaussian-Lorentzian function according to Beissinger et al. [49]; the mathematical equations of the functions can be found in reference [50]. As observed in **Table 4**, for all the cases after H charging, the ratio of the Cr oxide to Cr metal decreases considerably and the difference between the results obtained at 0.6mA/cm^2 and 5mA/cm^2 is negligible. The 625+ sample charged at 5mA/cm^2 shows a greater diminution in the Cr oxide percentage, which may have been a consequence of the decrease of the polarized surface area in a test conducted at constant charging current. We interpret this from a sudden potential change from ≈ -0.6 V_{SCE} to ≈ -1 V_{SCE} in the final hour of charging for this case. Nonetheless, the evolution of the oxide to metal ratio observed in Cr is similar for all the other oxides in the passive layer. It is worth noting that peaks presumably in the top surface of the bilayer i.e. NiO or $Ni(OH)_2$ show the same behaviour as the Cr oxide peaks, suggesting that the dissolution is not preferential in the top surface (see **Figure A.3**. in supplementary material). These results clearly identify that based on the decrease of the Cr-oxide signal, there is a measurable disruption to the air-formed passive layer on both alloys because of cathodic polarization.

Table 4. Analysis of the Cr $2p_{3/2}$ peak for alloys 718 and 625+ before and after cathodic polarization.

	718 before CP	**718 after CP at 0.6mA/cm^2**	**718 after CP at 5mA/cm^2**	**625+ before CP**	**625+ after CP at 0.6mA/cm^2**	**625+ after CP at 5mA/cm^2**
Cr metal (%)	37.02	79.05	79.07	38.45	80.69	89.81
Cr oxide (%)	62.98	20.95	20.93	61.55	19.31	10.19
Cr oxide/ Cr metal	1.70	0.26	0.26	1.60	0.24	0.11

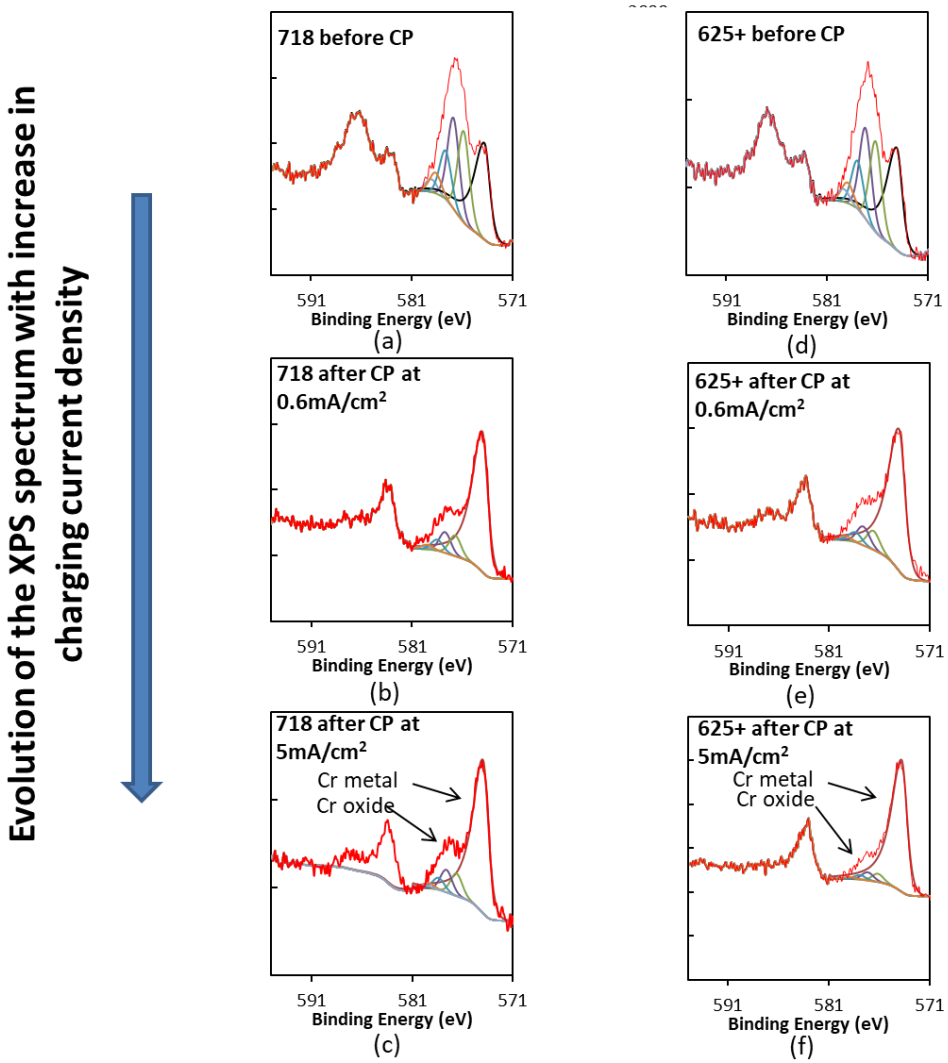

Figure 8. High resolution Cr 2p XPS spectra taken from the surface of the 2 alloys (a) 718 before charging, (b) 718 after charging at 0.6 mA/cm2, (c) 718 after charging at 5 mA/cm^2, (d) 625+ before charging, (e) 625+ after charging at 0.6 mA/cm^2 and (f) 625+ after charging at 5 mA/cm^2.

The analysis of the oxygen signal also confirms a decrease in the oxide signal observed in the Cr 2p peaks after polarization. **Figure 9** shows the progression of the oxygen signal with increase in the charging current density, for 718 at 5mA/cm^2 and 0.6mA/cm^2, and 625+ at 5mA/cm^2, the peak representing the lattice oxide is not present, for 625+ at 0.6mA/cm^2, the oxygen signal starts to increase in the region of the lattice oxide, however, the magnitude of this peak seems to be smaller compared to that observed in the condition before CP. The strong peak observed next to the oxide peak is a convolution of multiple signals which may include components such as structural water, residual sulphates (for samples exposed to 0.5M H_2SO_4), hydroxides and defective oxides [51-52].

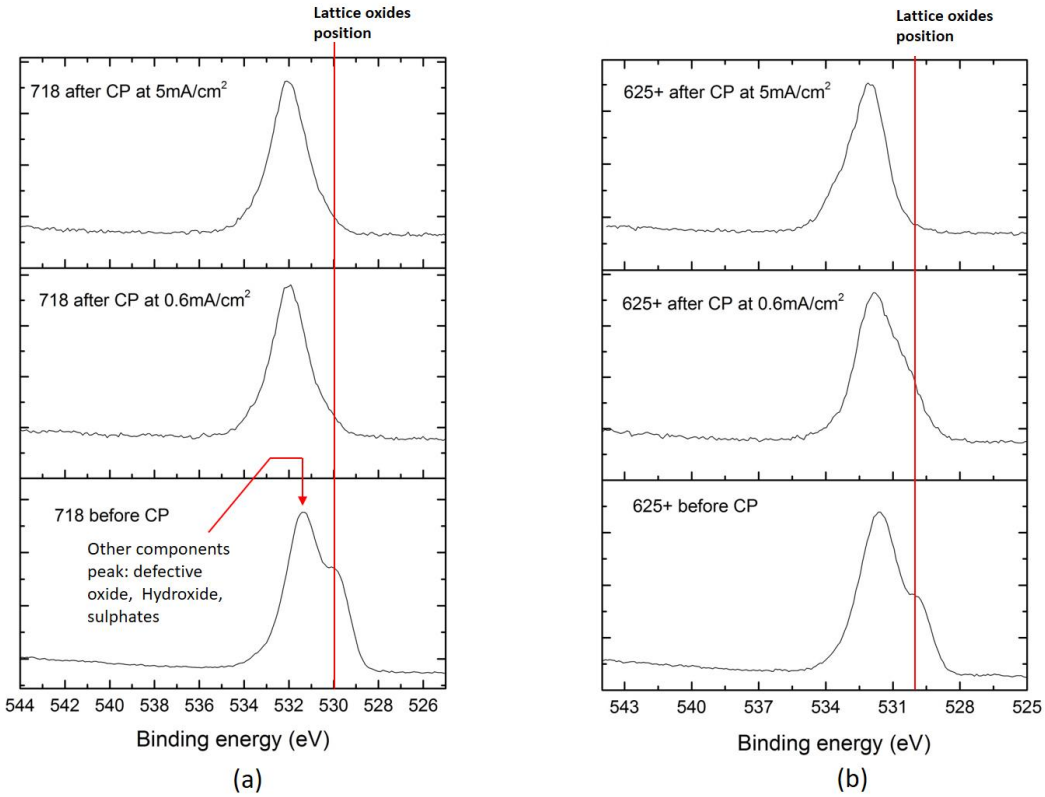

Figure 9. High resolution O1s XPS spectra taken from the surface of the 2 alloys (a) 718 and (b) 625+. Before and after H charging at 0.6 mA/cm^2 and 5mA/cm^2.

3.3. EIS results

Figure 10 presents the typical response observed in the Nyquist data for the different stages of **Figure 3** (EIS measurements at OCP in 1g/L NaCl or under cathodic polarization in H_2SO_4)[6]. This graph reveals a decrease in passive film protection after cathodic polarization. Prior to applying CP, the Nyquist plots show a capacitive behaviour with very high impedance with a straight line (~75°) at lower frequencies perhaps indicative of a species diffusion-controlled process. Regarding the Nyquist plots taken after charging, the impedance magnitudes are clearly lower and do not change over a 2h period. The magnitude of the impedances acquired *during CP* is very low and is shown as an inset within **Figure 10**. The time constants appear better defined, and quite likely relate to the rates of the faradaic reactions taking place at the surface of the electrode. Considering the strong acidic solution chemistry (pH = 0), we expect this to be a proton reduction reaction (PRR) under diffusion control at 5mA/cm², and under mixed activation-diffusion control at 0.6mA/cm² [53] for both alloys. In general, the Nyquist plots of 718 are like those obtained for 625+ i.e. the impedance magnitude is much larger before CP as compared to data acquired after CP.

[6] Figure 10 is taken from data obtained from 718 at a charging current density of 0.6mA/cm^2, however, this is rather like the behaviour observed in 625+ and to data obtained at 5mA/cm^2.

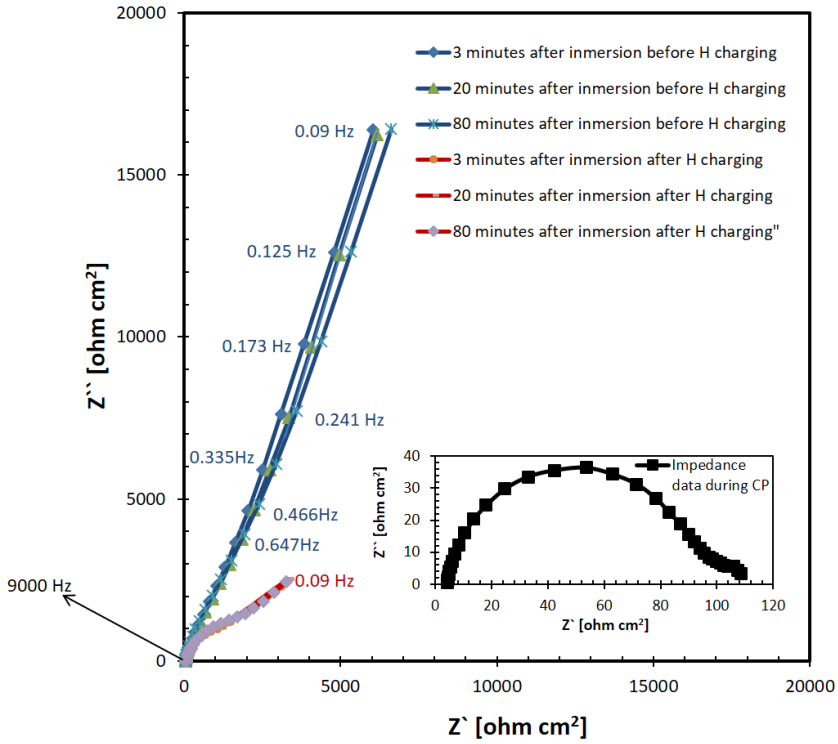

Figure 10. Nyquist Plot of alloy 718 in a solution of 1g/L NaCl at OCP before CP, and at OCP after CP, in a solution of 0.5M H_2SO_4 during CP at a charging current density of 0.6mA/cm^2. Examples of the fitted curves are included in the supplementary material **Figure A.3**.

In order to improve the EIS data interpretation and to build a physico-chemical model of the evolving interface that could be explained through a classical equivalent circuit analysis, the evolution of Bode plots (before, after and during CP) were also analysed; these are shown in **Figure 11**. Before CP in the 625+, the Phase angle data (**Figure 11(a))** display a very broad time constant at around -90° at low frequency (between 10 and 0.1 Hz) which indicates a highly capacitive, homogeneous, and compact interface. For 718, across the same frequency range, the phase angle is slightly higher and two time constants are evident, which suggest a slightly less capacitive interface for this alloy. Moving to data acquired during CP, the Bode plots appear to correspond to an active metal response, with high coherence between potential and current, suggesting a charge transfer process. However, we interpret that this cannot be related only to the dissolution of the passive film. Rather, the ratio of the impedances obtained between charging at the 2 different charging current densities is similar to the ratio of the applied charging current, which supports the suggestion that these "during CP" EIS data present information on the charge transfer kinetics of the proton reduction reaction. With respect to data acquired after CP, it is observed that the impedance and phase angle responses corresponding to the time constant at low frequency (10Hz – 0.1Hz) all diminish. The "after CP" interfacial response is not recovered, possibly since the Ni-base alloy samples were not re-exposed to air. Nonetheless, it is suspected that the loss of this low frequency contribution indicates a loss in the protective capability of the passive film.

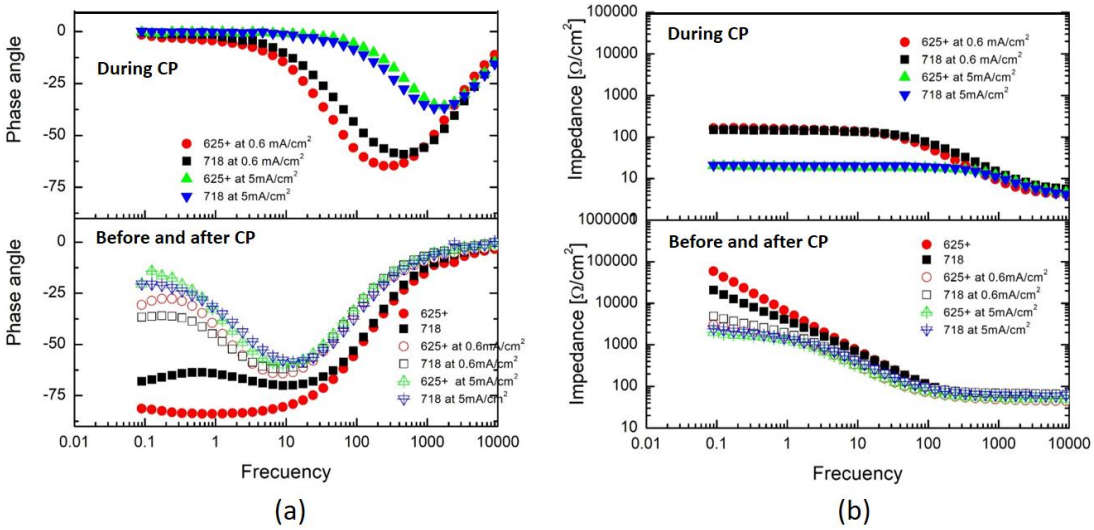

Figure 11. Bode Plots obtained from EIS in a solution of 1g/L NaCl at OCP before CP and after CP in a solution of 0.5M H_2SO_4 at two different charging current densities, the measurements were taken at OCP. During CP, the data was obtained in the solution of 0.5M H_2SO_4, and the data was obtained at the potential corresponding to the charging current density applied; (a) Phase angle versus frequency and (b) impedance versus frequency.

The equivalent circuit illustrated in **Figure 12** adequately models the impedance response of the system, with support from XPS data. Such a nested-model circuit is commonly used to model the interfacial behaviour of passive alloys in aqueous solutions [54-57]. A circuit composed of 2 resistance-constant phase element components (R-CPE) is used. This type of model is employed to represent the electrode surface and the heterogeneous passive layers [58-59], with the solution resistance R1 in series with the first time constant (R2-CPE1), where CPE1 represents the capacitance of the double layer and R2 corresponds to the kinetics of a charge-transfer process at the electrolyte/electrode interface. Based on XPS data, the passive layer of these alloys comprises different components, notably, oxides and hydroxides, assumed to be formed as a bilayer. By correlating the data to this model, if H charging affects the passive film, we expect that the changes may be reflected more strongly in the second resistance and capacitance outputs (CPE2-R3). The R3 parameter is very important in this case because we interpret it to be directly related to the characteristics of the passive film (or the passive Cr oxide to be more precise). Equation 1 was used to calculate the capacitance values C1 (solution/outer layer of alloy interface) and C2 (passive layer) [60], which could be used to estimate the thickness of the passive layer (δ) according to equation 2 [61-62]. The passive film thickness is taken to be inversely proportional to the capacitance, as expected for a parallel-plate capacitor type interpretation (Equation 2). **Table 5** shows the outputs of equivalent circuit model fitting outputs of the impedance data before and after CP. Since the shape and magnitude of the impedance curves do not vary considerably as a function of time in each stage, as can be observed in **Figure 10**, **Table 5** shows the average value for each parameter for this same equivalent circuit.

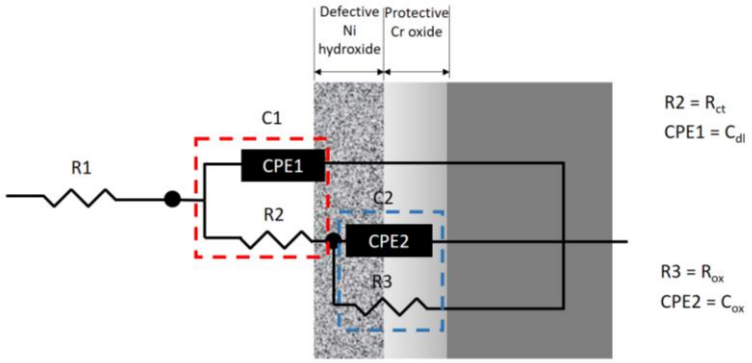

Figure 12. Equivalent circuit proposed to model the electrochemical behaviour of precipitation-hardened nickel-based alloys in a deaerated solution of 1g/L NaCl.

$$C = \frac{(QR)^{-}}{} \tag{1}$$

where Q represents the capacitive behaviour of a CPE, the exponent α indicates the behaviour of the CPE versus a perfect capacitor and R is the resistance of the different elements, R1, R2 and R3, in the circuit i.e. the resistance of an inner layer. The thickness (δ) of the passive layer is estimated accordingly as:

$$\frac{(\varepsilon\varepsilon_0)A}{} \tag{2}$$

where ε and ε_0 are the dielectric constants of the passive layer (we take the value of 30 for a passive Cr_2O_3 layer [61]), A is the interactive surface area and the permittivity of vacuum (8.8542 x 10^{-14} F/cm)respectively.

Table 5. Fitting parameters of the equivalent circuit presented in Figure 11 (averaged from minute 3 to minute 120). This was calculated in this way because the differences in impedance curves from minute 3 to minute 120 were very small, as observed in **Figure 10**. To model the EIS results for all testing conditions (before CP and after CP). The measurements were taken in a solution of 1 g/L NaCl. Chi-squared refers to the regression goodness of fit.

Alloy	Condition	R_1 [Ω cm^2]	R_2 [Ω cm^2]	R_3 [Ω cm^2]	α_1	α_2	C_1 [μF/cm^2]	C_2 [μF/cm^2]	δ (inner film) [nm]	Chi-Squared
718	Before CP	44.12	6074	142032	0.88	0.88	32.7	46.1	5,7	0.0012
	After CP at 0.6mA/cm^2	57.385	2730	4680	0.85	0.96	73.06	489	0.5	0.00058

	After CP at 5mA/cm^2	50.92	1437	1009	0.85	0.95	75.37	1816.6	0.14	0.0036
625+	Before CP	49.83	6997	1873168	0.98	0.88	18.06	20.9	12,6	0.044
	After CP at 0.6mA/cm^2	43.89	2041	4025	0.86	0.98	65.66	1129,1	0,2	0.0025
	After CP at 5mA/cm^2	48.36	1308	1220	0.86	0.98	75.03	3284.6	0.08	0.0013

From the analysis of the data for the alloys before applying cathodic polarisation, the value of R3 is extremely large. We recall that the passivity is understood to arise mainly from the inner Cr-oxide rich film. R3 is higher for alloy 625+ than for alloy 718, an expected observation since the former alloy is known to possess higher corrosion resistance [63]. The values of R2 are similar for both alloys, due to the similar surface preparation features, and what we believe to be comparable double layer/ outer surface film structure contributions. The C2 capacitance value is lower in alloy 625+ than in 718, which could be a reflection of a slightly thicker passive film in 625+.The values of the capacitance suggest a film thickness between ≈5nm and ≈13 nm, for 718 and 625+ respectively. Upon evaluating the high-mid frequency range (10 kHz to 10Hz) in the Bode plots in **Figure 11**, the double layer time constant response is similar before and after cathodic polarization. After cathodic charging, the C1 values are noted to simply double in magnitude irrespective of the magnitude of applied CP current density for alloy 718; they increase approximately by a factor of 4 for alloy 625+. The more dramatic changes are observed to the second time constant C2 and resistance R3, in the mid-low frequency range (10 Hz to 100 mHz). The R3 values decrease by orders of magnitude after cathodic polarization, compared to R2. This decrease is most significant at 5 mA/cm². Looking at the capacitance data, the C2 capacitances increase by one order of magnitude at 0.6 mA/cm² and two orders of magnitude at 5 mA/cm² .This C2 capacitance is strongly expected to change as a result of passive oxide film thinning or dissolution resulting in a massive increase in surface area (which could leave a porous base structure). With the C2 evaluated alongside the drastic decrease in R3, it suggests that this time constant represents the corrosion-protective nature of the passive film (which appears to be uniformly thinned during the cathodic polarisation step).

Our EIS interpretations are supported by XPS data. After polarization, the XPS data presented in **Figure 9** reveal a decrease in the peaks of all oxides from both alloys, which correlates with the reduction in the R3 values (corrosion protection) and reflects thinner passive films. The relative insensitivity of the first, higher frequency time constant C1 -R2 is attributed to dielectric changes in the outer surface of the passive film and different rates of the proton reduction reaction. In terms of the dissolution of the passive layer, both XPS and EIS measurements suggest that the dissolution of the passive layer is more significant at higher charging current densities. According to the XPS measurements, the dissolution of the passive layer of alloy 718 is no different between 0.6mA/cm^2 and 5mA/cm^2. However, based

on electrochemical measurements, R3 which is related to the passive layer, shows a greater decrease at 5mA/cm^2 than at 0.6mA/cm^2 for both alloys.

As well as the XPS and EIS analysis, which both suggest a modification to the passive layer, it is relevant to examine the open circuit potential (OCP) transients. In deaerated 1g/L NaCl during these measurements, see **Figure 13**. The potential values were more negative for the same sample after H charging, indicative of a more electrochemically active surface. Nonetheless, they appear to return towards the more noble, original OCP values**.** Finally, we should highlight that none of these techniques confirm a *complete* dissolution of the passive layer.

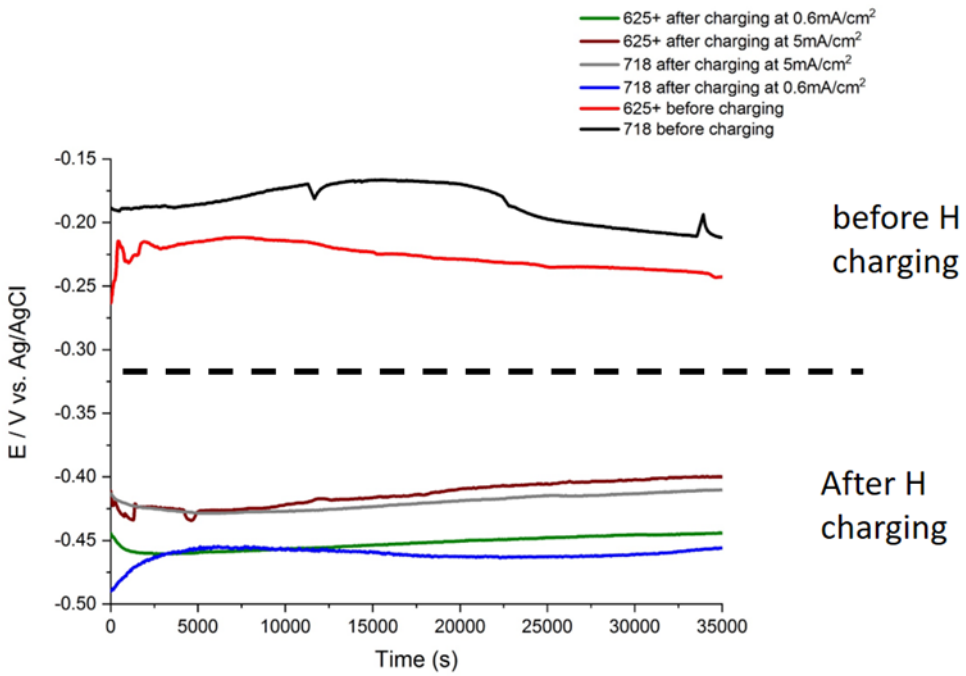

Figure 13. OCP values before and after charging in a solution of H_2SO_4. The measurements were obtained in a solution of 0.017M NaCl.

From the point of view of the corrosion properties, many articles in the literature support the suggestion that an increase in H-adsorption/uptake could increase a passive alloy's susceptibility to pitting corrosion and decrease the stability of the passive layer, e.g. [64-67]. Some arguments for these phenomena are related to a chemical reaction occurring at the surface of the working electrode. i.e. iron reduction from Fe^{3+} to Fe^{2+} [68]. The deleterious effect of H in the corrosion properties has been seen in other pure elements such as Ni and other alloys, such as UNS N08031 and 316L stainless steel (EN 1.4462) [67]. In the presence of Mo, adsorbed H can cause fast reduction of Mo^{6+} to Mo^{5+} [43].

For the case of Cr_2O_3 films, Schmuki *et al.* [69] found during *in situ* X-ray Near Edge Spectroscopy measurements (XANES) under cathodic polarization conditions (0.1M H_2SO_4, and also in alkaline solutions with Cr_2O_3 content below 10%), that films containing below 50% Cr_2O_3 experience film dissolution via detachment of the matrix. Kim *et al* found similar results in artificial mixed Fe_2O_3 - Cr_2O_3 films [70].

The results obtained from the XPS and the impedance measurements of this research have suggested that varying the H_{ads} activity (0.6 mA/cm² or 5 mA/cm²) causes deterioration of the passive layer to varying extent. To understand the effects of H_{ads} at the surface of metals, Flis et al. [71] conducted AFM measurements of the surface of pure Fe after different charging times in a solution of 0.1M NaOH at a cathodic current density of 10mA/cm^2. They observed that after 1 h of H-charging the polishing marks become sharper, with the changes in the surface becoming more prominent with time. They attributed this to the disappearance (reductive chemical dissolution) of surface iron oxides. Equally, Maurice et al observed changes in the surface of a Cr(110) single crystal after cathodic polarization for 5 minutes in a solution of 0.5M H_2SO_4 at 5mA/cm^2 and assigned the topographical changes to hydride formation [72]. Tamm et aI. [73] suggested that surface modification may have been caused by mechanical damage due to H evolution.

In our experiments, samples were ground and polished and then charged using the same conditions as used in the mechanical tests and in the glove box tests (12 hours of cathodic H charging in a deaerated solution of 0.5 M H_2SO_4 at a current density of 5 mA/cm^2) to observe changes at the surface. After charging, the samples were also exposed to the atmosphere to be analysed by an Atomic Force Microscope (AFM), and a laser confocal microscope. In the samples ground to 1200 grit paper, no differences were observed in the surfaces due to the relatively high roughness produced by the grinding process. Other samples were analysed before and after charging by the laser confocal microscopy after polishing to 1 µm OPS finishing (see supplementary material, **Figure A.5**). In this case, although differences in roughness of the surface line profiles were seen, they are attributed to be background noise, the differences are beyond the resolution of the equipment. Considering the information found in the literature, it is not unreasonable that numerous mechanisms, acting individually or simultaneously, could be responsible for causing the dissolution and degradation of the passive layer in our studied nickel alloys. These may include the reduction of Fe^{3+} to Fe^{2+} [68], chemical dissolution, hydride formation [72], mechanical distortion caused by H evolution[7] [73], and local potential difference corrosion cells [74]. On the other hand, the equivalent circuit of **table 5** shows that after hydrogen charging, a near perfect capacitance for C2 (see values of α_2) is attained, which suggests a high level of homogeneity in the passive layer. This may support the idea that the passive layer could be thinned i.e. via a surface complexation-type dissolution mechanism [75], resulting in the formation of passive film islands and thinning of the passive layer, as schematically illustrated in **Figure 14.**

In summary, our EIS and XPS results indicate that even a cathodic current density of 0.6 mA/cm² is sufficient to considerably depassivate/weaken the surface passive film structure and permit a certain quantity of hydrogen entry.

[7] The reason behind this was not described in the paper.

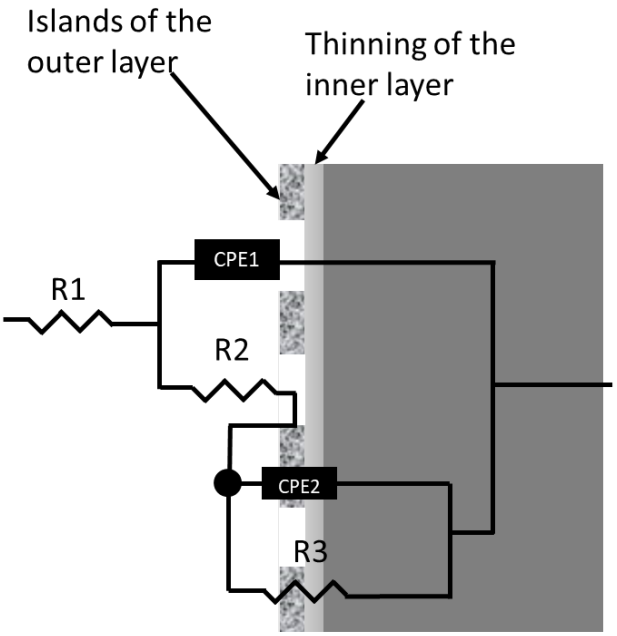

Figure 14. Schematic illustration of a possible interfacial structure that corresponds to the various impedance responses during CP, i.e. the partial reduction/dissolution of the passive film.

3.4. Interpretation of Mechanical results in relationship to electrochemical observations

Before correlating the effects of passive film dissolution to the changes in the mechanical cracking properties, it should be noted that the time variable in the film dissolution is unknown i.e. the initial steps in the RSLTs are far shorter than 12 hours. Based on the data obtained from the mechanical tests (**Figure 5**), and comparing a conventional SSRT with the modified RSLT technique, the results can be divided into two categories: (i) tests where the time to failure was different (718 at 0.6mA/cm^2) and (ii) tests where the time to failure was similar for both methodologies (718 at 5mA/cm^2, and 625+ at both 0.6mA/cm^2 and 5mA/cm^2). The small difference in the time to failure obtained from the SSR and RSL tests may be explained based on the effects of CP which deteriorates the passive layer of the Ni-base alloys.

For Alloy 718, charged at 0.6mA/cm^2 (case (i)), the differences between the SSR and the RSL tests are possibly down to dissimilarities in the crack growth (crack growth stage) occurring in the two methodologies, rather than during crack nucleation alone (i.e. role of the passive layer decreasing hydrogen uptake). **Table 6** shows the time to failure for both methodologies, including the crack nucleation time from the RSLTs. Crack nucleation times were estimated in the RSLTs from the shape of the falling step upon reaching the defined stress in the stress vs. time curves [76]. Typically, failure was observed to follow shortly after the crack nucleation process, apart from 718 at 0.6mA/cm^2.

Table 6. Crack nucleation and time to failure for the SSR and the RSL tests, including time difference between crack nucleation time and time to failure.

	718 SSRT 0.6 mA/cm^2(h)	718 RSLT 0.6 mA/cm^2 (h)	718 SSRT 5 mA/cm^2(h)	718 RSLT 5 mA/cm^2(h)	625+ SSRT 0.6 mA/cm^2(h)	625+ RSLT 0.6 mA/cm^2(h)	625+ SSRT 5 mA/cm^2(h)	625+ RSLT 5 mA/cm^2(h)
Crack nucleation	N\D	55.9	N\D	22	N\D	17.9	N\D	26.1
Time to failure	41.5	70	23.8	23.4	15.7	19.4	27.09	29.5
Time difference	N\D	14.1 (20%)*	N\D	1.4 (5.9%)*	N\D	1.5 (7.7%)*	N\D	3.4 (11.5%)

The time to failure was defined as the time when the load has fallen more than 85%. *indicates the percentage of time in a test for crack growth until test failure.

The general discussion is supported with fractography results, **Figure 15** and **17** and complementary SSRTs, presented in **Figures 16**. For the case of alloy 625+ which exhibits higher susceptibility to HE at low charging current densities during the conventional SSRT, the analysis of the fracture surface after 0.6mA/cm^2 charging shows completely intergranular cracking behaviour, even at the centre of the specimen (**Figure 15(a)**). This homogeneity for the entire fracture surface is interesting and may result from the fact that electrochemical interactions inside the cracks are comparable to those near the surface of the specimens. This is rather unexpected due to the IR drop effect [16]. It may indicate that the Cr-Mo precipitates decorating the grain boundaries play a very important role in the HE of 625+, as weak reversible H traps, or as electroactive sites permitting H-entry. Indeed, they may also behave as a catalyst to the hydrogen evolution reaction (rather than H-entry). Concerning the 625+ SSRT specimen charged at -5mA/cm^2, **Figure 15(b)**, intergranular/transgranular cracking with quasi-cleavage reminiscent features are noted. Such a different post-SSRT fracture morphology must be indicative of lower H uptake at the crack tip [18] at high (5mA/cm^2) charging current density, with the crack growth promoted partially by HE and partially by the high stresses in the remaining ligaments. During SSRT, the continuous straining continually increases the applied stress as a function of the strain hardening of the material [77].

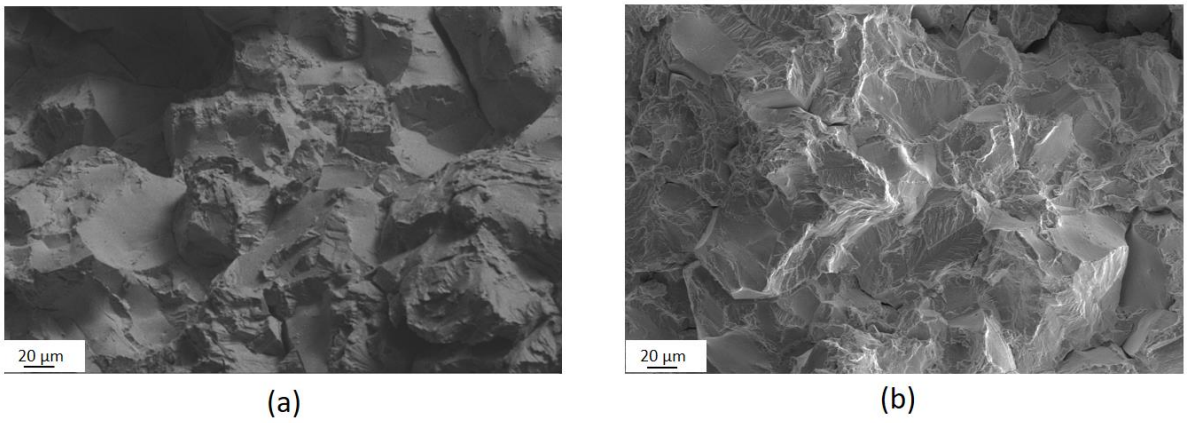

Figure 15. SEM images taken in the centre of the fracture surface of the SSRT in alloy 625+ polarized at (a) -0.6mA/cm^2 and (b) at -5mA/cm^2.

Complementary tests were conducted as a first attempt to find evidence to explain the reduced time to failure of 625+ at lower charging current density. Lillard et al. [16] found that in a 718 alloy in SEN specimens in a particular microstructural condition, the values of K_{th} reached a lower value at intermediate potentials in tests conducted in acidic solutions; they attributed this increase in K_{th} at more negative potentials to the decrease in H production due to an increase in the alkalinity at the crack tip. Taking as a baseline the Lillard et al. [16] results, a number of additional SSRTs were conducted to examine the influence in the time to failure of the treatment conditions of 625+. New electrochemical conditions were also chosen for these tests, to find out if another differentiating parameter could play a role i.e. temperature or solution chemistry. The new SSRTs were conducted in a solution of 3.5 wt% NaCl with pH modified to 8.5 at 80°C. The new microstructural condition of 625+ has been presented in previous communications, see references [20,21], with respect to the main microstructure studied in this paper. Specifically, two microstructural conditions are different in the new alloy: (i) the morphology of γ' and γ'' and (ii) redistribution of grain boundary precipitates i.e. after the solution annealing heat treatment (Intermediate step between both heat treatments), the grain boundary is decorated only with white compact particles (BSE detection) rich in Mo and Cr. These are structurally different to the elongated black and white Mo and Cr precipitates observed in inset of **Figure 2(b)**. **Figure 16** shows the results of the tests conducted in the new conditions at 0.5mAcm^2 and 1mA/cm^2. For the 625+ with new microstructural condition, the time to failure decreases with the increase in the charging current density, as in the case of 718. However, for the "conventional microstructure" 625+, the time to failure shows the same pattern to that observed in tests conducted in the 0.5M H_2SO_4 solution.

Once again, this demonstrates the important role played by the grain boundary precipitates in 625+. It should be noted that in the case of 625+, the fracture path is mainly intergranular, and so the electrochemical interactions occurring within the crack, such as the cathodic reactions and the sites available for hydrogen uptake, must be completely different to those observed in the bulk of the specimen i.e. local hydrogen enrichments were found at the grain boundary precipitates of alloy 625+ using NanoSIMS [21].

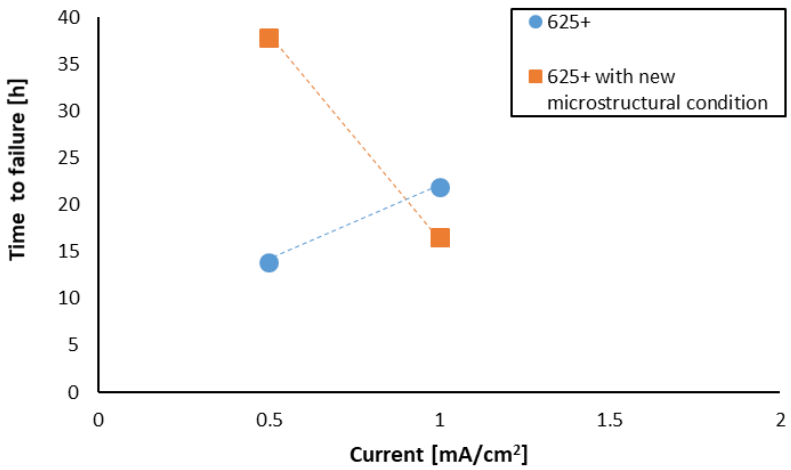

Figure 16. Time to failure *vs.* charging current density obtained for 625+ from SSRTs conducted in a solution of 3.5 wt% NaCl with pH modified to 8.5 at 80°C in two different microstructural conditions.

For alloy 718 charged at 0.6mA/cm^2 during RSLT**, Table 6** shows that there is a notable delay in the time to failure, after crack nucleation. Such a delay could signify a lower HE susceptibility under the studied conditions being, at least partially, linked to H uptake at the crack tip (during the crack propagation stage)[8]. This result is supported by the fracture surface images in **Figure 17**. Here, it is noted that in the RSLT 718 charged at 0.6mA/cm^2, **Figure 17(a),** the failure is driven by void nucleation at the centre of the specimen (ductile failure driven). This observation contrasts with other specimens, which have shown extensive regions of brittle failure with small microvoids in the centre of the specimen including the post-SSRT images of alloy 718 charged at 0.6mA/cm^2, **Figure 17(b).**

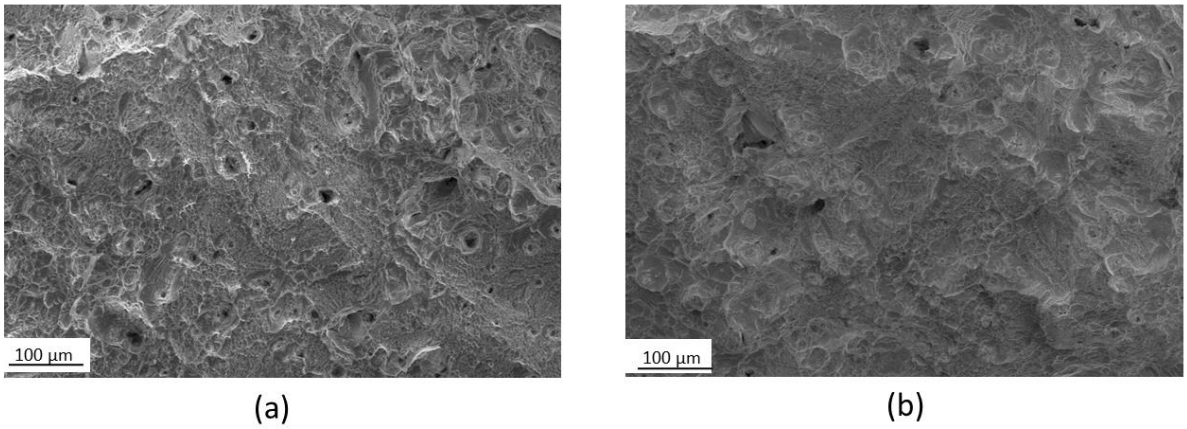

[8] Alternatively, the difference in crack nucleation times could be due to the interpretation of the load displacement diagram, the time determination for crack initiation in the RSLTs is based on standard ASTM F1624 in which tests are conducted on notched specimens (as opposed to smooth specimens such as those used in our study)

Figure 17. SEM images of the fracture surface of alloy 718 in the centre of the specimen polarized at -0.6mA/cm^2 from (a) the RSLT and (b) the SSRT.

The results presented so far show the potential role of slower localized H uptake kinetics (at the crack tip) as an explanation for the delayed time to failure in the hydrogenating environment for Alloy 718. However, crack tip uptake of hydrogen cannot be considered as the only variable playing a role. For instance, in the case of Alloy 718, the RSLTs at different charging current display a noticeable difference in the crack nucleation times. From this, we suspect that there may be different H-uptake and concentration profiles as a function of the cathodic current density. This could be expected as subsurface H concentration is found to be proportional to the square root of the applied current density [24]. Since no irreversible traps are reported for these alloys [78], the total H concentration in the bulk material is either reversibly trapped H or freely diffusible in the lattice. The H concentration data, presented in **Figure 18 (a)** and **(c)**, appear to indicate a very weak correlation between total H content and time to failure. However, on closer inspection, we evaluate that: (i) the large scatter in some of the results may be driven by local uptake from the fracture surfaces in secondary cracks and (ii) the test with lowest H content (718 RSLT charged at 0.6mA/cm^2) shows the longest time to failure. This second trend becomes even clearer when the hydrogen content is normalized as a function of the time to failure, whereby this normalization considers the longer cathodic polarisation times in the longer tests. For 718, **Figure 18 (b) and (d)** show that the two cases with lower normalized H content show longer times to failure. Similarly, in 625+, the same analysis confirms that the case with lower normalized H content (RSLT at 5 mA/cm²) also displays the longer time to failure.

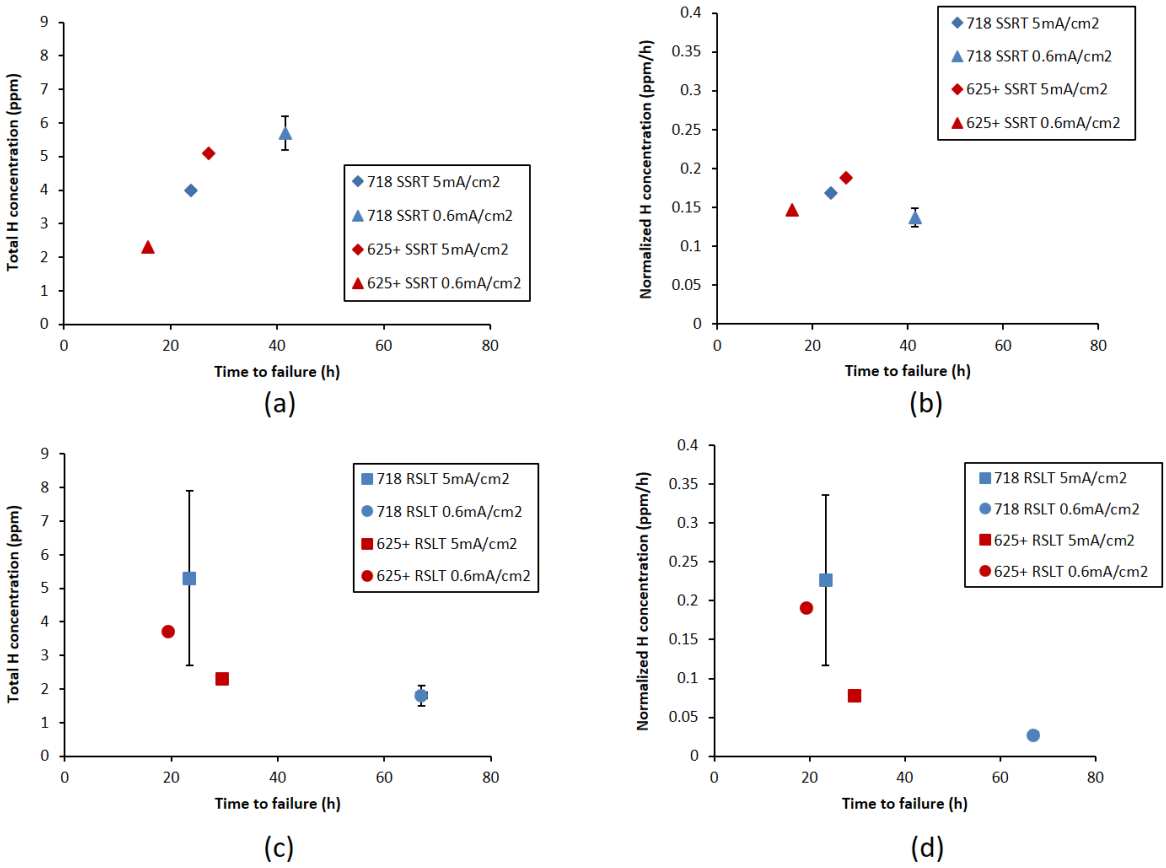

Figure 18. Hydrogen concentration as function of the time to failure of the specimens (≈ to the charging time). (a) Total H concentration (ppm) for SSRTs, (b) Hydrogen concentration normalised to charging time to failure (ppm/h) for SSRTs, (c) Total H concentration (ppm) for RSLTs and (d) Hydrogen concentration normalised to charging time to failure (ppm/h) for RSLTs.

On the other hand, a rather interesting observation can be made by comparing the SSRTs of 625+ at 5 mA/cm^2 and 0.6 mA/cm^2 (**Fig. 18 (a-b)**). The test carried out at 0.6 mA/cm^2 shows lower normalized hydrogen content than the test at 5 mA/cm^2. It appears that a higher current density certainly contributes to the thinning of the passive layer[9]. However, we have attained 625+ cracking earlier for the former, lower current density case, see **table 6**. Combining this evidence, with the results of the mechanical tests in the 625+, highlights the significance of the microstructure in the hydrogen local uptake. Here, two simultaneous conditions are thought to be attained and these can be used to explain the higher susceptibility to hydrogen embrittlement of 625+ at lower i_c: (i) based on the fracture surface images, a very low critical hydrogen concentration is required for HE emanating from the grain boundary decorated precipitates of conventional 625+ and (ii) a possibly lower hydrogen uptake at higher i_c, a function of surface reaction control. Based on the results of this study, the causes of the higher localised uptake at lower i_c are quite likely related to the GB precipitates. Speculatively, at higher $i_{c,}$ other secondary reactions could be more active, for example, XPS analysed showed some copper electrodeposition for all the conditions studied (see supplementary **Figure A.6**). Other conditions which could hinder the hydrogen uptake at higher i_c could be related to an increase in the bulk interfacial alkalinity because of the reduction reactions.

Interestingly, the RSLTs appear to correlate the normalized hydrogen concentration with time to failure quite well, **Figure 18(d),** where local uptake through film rupture is minimized. It should be noted that lower bulk hydrogen concentration at higher i_c in the RSLTs of 625+ was not expected. In terms of using the RSLT for material qualification purposes, one aspect that should be considered is the role of the charging current density. Lower values of i_c are better suited for qualification purposes as they produce larger differences in time to failure between both materials. The role of applied potential in discerning the effect of microstructural parameters in HE susceptibility are discussed in references [79-80].

Based on the fracture surface analysis, the failure of the RSLT of 718 at 0.6mA/cm^2 is driven by ductile damage. Note: it is expected that the alloy 718 used in this study, with the applied heat treatment, should result in a condition with low HE susceptibility [11, 19-20]. **Figure 18 (b)** and **(d)** also support the idea that this modified RSLT methodology could be more appropriate and more sensitive than the SSRT methodology for qualifying purposes. It offers a consistent and larger differentiation in the hydrogen content inside the specimens compared to the hydrogen content measurements in the SSRT specimens; this is presumably related to continuous uptake of hydrogen in the active sites during SSRTs, whether it is by dynamic

[9] It should be noted that real H-uptake measurements were not taken in this study i.e. subsurface hydrogen concentration measurements (C_o) from permeation studies as a function of the charging current density.

straining and rupture of the passive layer or local uptake though active crack tip sites, resulting in a minimization of the role of the microstructural features.

Conclusions

We have modified the RSLT test by incorporating interrupted electrochemical hydrogen charging, and compared the results against the conventional SSRT methodology, to determine the relevance of continuous straining as a factor in the assessment of the susceptibility of nickel-based alloys 625+ and 718 to hydrogen embrittlement. The main findings from this study are summarized below.

- RSLT and SSRT assessments generally show similar results at first glance, notably longer times to failure at lower charging current density for 718 and vice versa for 625+;
- Glovebox XPS and EIS experiments both offer evidence of partial passive layer dissolution during cathodic protection in an acidic solution at both charging current densities, which may explain why there were fewer differences between the results of both mechanical testing methodologies;
- Although Alloy 625+ proved to be more susceptible to HE than 718 from bulk mechanical testing results, the global measurements of the dissolved hydrogen concentration demonstrate that these differences were not attributed to a higher total hydrogen concentration in 625+; It was proposed rather to be due to preferential localised hydrogen uptake at conducive grain-boundary features in 625+
- The differences in the crack nucleation times suggest that the susceptibility to HE during a SSR test is not particularly sensitive to hydrogen uptake at the crack tip;
- Concerning the results of alloy 718 charged at 0.6mA/cm^2, this could be considered the perfect example to prove that continuous straining in the presence of hydrogen can enhance the HE susceptibility response. In this respect, SSRT may not be the most appropriate method for assessment of an HE mechanism for passive alloys.

Acknowledgments

The authors would like to acknowledge the funding and technical support from BP through the BP International Centre for Advanced Materials (BP-ICAM) that made this research possible. Special thanks to Ben Spencer and Monika Walczak who helped acquire the XPS data.

References

1 Shademan, S. S., Martin, J. W., & Davis, A. P. (2012, January). UNS N07725 nickel alloy connection failure. In *CORROSION 2012*. NACE International.

2 Kulawik, K., Buffat, P. A., Kruk, A., Wusatowska-Sarnek, A. M., & Czyrska-Filemonowicz, A. (2015). Imaging and characterization of γ′ and γ ″nanoparticles in Inconel 718 by EDX elemental mapping and FIB–SEM tomography. *Materials Characterization*, *100*, 74-80.

3 Vander Voort, G. F., Bowman, J. W., & Frank, R. B. (1994). Microstructural characterization of custom age 625 plus alloy. *Superalloys*, *718*, 625-706.

4 Fairhurst, D. (2003). Offshore cathodic protection. What we have learnt. *Journal of Corrosion Science and Engineering*, *4*, 6.

5 Krishnan, T., Rooker, J., & Chitwood, B. (2009, January). Case-history of environmental cracking failures with alloy K-500 for downhole completion tools. In *CORROSION 2009*. NACE International.

6 Nice, P., Strong, R., Bailey, W. M., Rørvik, G., Olsen, J. H., & Mobberley, T. G. (2014, May). Hydrogen embrittlement failure of a precipitation hardened nickel alloy subsurface safety valve component installed in a North Sea seawater injection well. In *CORROSION 2014*. NACE International.

7 Campbell, H. S., & Francis, R. (1995). Simulated service test for hydrogen embrittlement of cathodically protected subsea bolting materials. *British Corrosion Journal*, *30*(2), 154-162.

8 Zhang, Z., Obasi, G., Morana, R., & Preuss, M. (2016). Hydrogen assisted crack initiation and propagation in a nickel-based superalloy. *Acta Materialia*, *113*, 272-283.

9 Galliano, F., Andrieu, E., Blanc, C., Cloue, J. M., Connetable, D., & Odemer, G. (2014). Effect of trapping and temperature on the hydrogen embrittlement susceptibility of alloy 718. *Materials Science and Engineering: A*, *611*, 370-382.

10 Kagay, B. J. (2016). *Hydrogen embrittlement testing of alloy 718 for oil and gas applications* (Doctoral dissertation, Colorado School of Mines. Arthur Lakes Library).

11 Demetriou, V., Robson, J. D., Preuss, M., & Morana, R. (2017). Study of the effect of hydrogen charging on the tensile properties and microstructure of four variant heat treatments of nickel alloy 718. *international journal of hydrogen energy*, *42*(37), 23856-23870.

12 Sampath, D., Akid, R., & Morana, R. (2018). Estimation of crack initiation stress and local fracture toughness of Ni-alloys 945X (UNS N09946) and 718 (UNS N07718) under hydrogen environment via fracture surface topography analysis. *Engineering Fracture Mechanics*, *191*, 324-343.

13 Obasi, G. C., Zhang, Z., Sampath, D., Morana, R., Akid, R., & Preuss, M. (2018). Effect of microstructure and alloy chemistry on hydrogen embrittlement of precipitation-hardened Ni-Based alloys. *Metallurgical and Materials Transactions A*, *49*(4), 1167-1181.

14 Wang, C. P., Yu, G. P., & Huang, J. H. (1996). *The effects of heat treatment and hydrogen on the SCC behavior of superalloy 718* (No. CONF-960389-). NACE International, Houston, TX (United States).

15 Hicks, P. D., & Altstetter, C. J. (1990). Internal hydrogen effects on tensile properties of iron- and nickel-base superalloys. *Metallurgical Transactions A*, *21*(1), 365-372.

16 Lillard, J. A., Kelly, R. G., & Gangloff, R. P. (1997). Effect of electrode potential on stress corrosion cracking and crack chemistry of a nickel-base superalloy. In *Corrosion/97 conference papers*.

17 Kernion, S. J., Magee, J. H., Heck, K. A., & Werley, T. N. (2015, May). Effect of microstructure and processing on the hydrogen embrittlement of Ni-base superalloys. In *CORROSION 2015*. NACE International.

18 Gangloff, R. P., Ha, H. M., Burns, J. T., & Scully, J. R. (2014). Measurement and modeling of hydrogen environment-assisted cracking in Monel K-500. *Metallurgical and Materials*

Transactions A, *45*(9), 3814-3834.

19 Foroni, L., & Malara, C. (2014, March). Hydrogen embrittlement susceptibility of precipitation hardened Ni-alloys. In CORROSION 2014. OnePetro.

20 Martelo, D. F., Morana, R., & Akid, R. (2021). Understanding the mechanical behaviour of 718 and 625+ nickel based super-alloys under cathodic polarization. Theoretical and Applied Fracture Mechanics, 112, 102871.

21 Aboura, Y., Martelo, D. F., Morana, R., Akid, R., & Moore, K. L. (2021). Characterising hydrogen induced cracking of alloy 625+ using correlative SEM-EDX and NanoSIMS. *Corrosion Science*, *181*, 109228.

22 DeMott, R. W., Kernion, S., Leff, A. C., & Taheri, M. L. (2021). Mitigation of hydrogen embrittlement in alloy custom age 625 PLUS® via grain boundary engineering. Materials Science and Engineering: A, 818, 141377.

23 Barnoush, A. (2011). Hydrogen embrittlement. *Saarland University*.

24 A. Turnbull. Hydrogen diffusion and trapping in metals. In Gaseous Hydrogen Embrittlement of Materials in Energy Technologies: Mechanisms, Modelling and Future Developments (pp. 89-128). Gangloff, R. P., & Somerday, B. P. (Eds.). (2012). Gaseous hydrogen embrittlement of materials in energy technologies: mechanisms, modelling and future developments. Elsevier.

25 Takeda, M., Kurisu, H., Yamamoto, S., & Nakagawa, H. (2009). Hydrogen distribution in titanium materials with low outgassing property. *Vacuum*, *84*(2), 352-356.

26 Kussmaul, K., Blind, D., & Läpple, V. (1997). New observations on the crack growth rate of low alloy nuclear grade ferritic steels under constant active load in oxygenated high-temperature water. *Nuclear engineering and design*, *168*(1-3), 53-75.

27 Liu, X., Hwang, W., Park, J., Van, D., Chang, Y., Lee, S. H., ... & Lee, B. (2018). Toward the multiscale nature of stress corrosion cracking. *Nuclear Engineering and Technology*, *50*(1), 1-17.

28 Griffiths, A. J., & Turnbull, A. (2001). Defining the limits of application of duplex stainless steel coupled to carbon steel in oilfield environments. *Corrosion*, *57*(2), 165-174.

29 Sampath, D. BP-ICAM Annual Year report. ICAM 04. 2017

30 McCoy, S. A., Mannan, S. K., Tassen, C. S., Maitra, D., & Crum, J. R. (2015, May). Investigation of the effects of hydrogen on high strength precipitation hardened nickel alloys for O&G service. In *CORROSION 2015*. NACE International.

31 Stenerud, G. (2014). *The susceptibility to hydrogen induced stress cracking for alloy 718 and alloy 725* (Master's thesis, Institutt for produktutvikling og materialer).

32 Rollins, B. C., Thodla, R., Carlton, C. J., & Paes, M. P. (2016). Development of test methodology to evaluate high strength nickel based alloys under cathodic protection. In *NACE International Corrosion Conference Proceedings* (p. 1). NACE International.

33 Henthorne, M. (2016). The slow strain rate stress corrosion cracking test—a 50 year retrospective. *Corrosion*, *72*(12), 1488-1518.

34 Schmidt, N. B., DeBold, T. A., & Frank, R. B. (1992). Custom age 625® plus alloy—A higher strength alternative to alloy 625. *Journal of Materials Engineering and Performance*, *1*(4), 483-

488.

35 TM0198, N. A. C. E. (2004). Slow strain rate test method for screening corrosion-resistant alloys (CRAs) for stress corrosion cracking in sour oilfield service. *Houston, TX: Nace*.

36 Test procedure to assess the susceptibility of PH nickel base alloys to hydrogen embrittlement - TOTAL. 2012, Institut de la Corrosion.

37 Cialone, H., & Holbrook, J. (1988). Sensitivity of steels to degradation in gaseous hydrogen. In Hydrogen embrittlement: prevention and control. ASTM International.

38 Walczak, M. S., Morales-Gil, P., Belashehr, T., Kousar, K., Lozada, P. A., & Lindsay, R. (2017). Determining the chemical composition of corrosion inhibitor/metal interfaces with XPS: minimizing post immersion oxidation. *JoVE (Journal of Visualized Experiments)*, (121), e55163.

39 Morales-Gil, P., Walczak, M. S., Cottis, R. A., Romero, J. M., & Lindsay, R. (2014). Corrosion inhibitor binding in an acidic medium: Interaction of 2-mercaptobenizmidazole with carbon-steel in hydrochloric acid. *Corrosion science*, *85*, 109-114.

40 Biesinger, M. C., Payne, B. P., Grosvenor, A. P., Lau, L. W., Gerson, A. R., & Smart, R. S. C. (2011). Resolving surface chemical states in XPS analysis of first row transition metals, oxides and hydroxides: Cr, Mn, Fe, Co and Ni. *Applied Surface Science*, *257*(7), 2717-2730.

41 Bakare, M. S., Voisey, K. T., Roe, M. J., & McCartney, D. G. (2010). X-ray photoelectron spectroscopy study of the passive films formed on thermally sprayed and wrought Inconel 625. *Applied Surface Science*, *257*(3), 786-794.

42 Baltrusaitis, J., Mendoza-Sanchez, B., Fernandez, V., Veenstra, R., Dukstiene, N., Roberts, A., & Fairley, N. (2015). Generalized molybdenum oxide surface chemical state XPS determination via informed amorphous sample model. *Applied Surface Science*, *326*, 151-161.

43 Borgschulte, A., Sambalova, O., Delmelle, R., Jenatsch, S., Hany, R., & Nüesch, F. (2017). Hydrogen reduction of molybdenum oxide at room temperature. *Scientific reports*, *7*, 40761.

44 Grundner, M., & Halbritter, J. (1980). XPS and AES studies on oxide growth and oxide coatings on niobium. *Journal of Applied Physics*, *51*(1), 397-405.

45 Neville, A., & Hodgkiess, T. (2000). Study of passive film on stainless steels and high grade nickel base alloy using X-ray photoelectron spectroscopy. *British Corrosion Journal*, *35*(3), 183-188.

46 Marcus, P., & Grimal, J. M. (1992). The anodic dissolution and passivation of NiCrFe alloys studied by ESCA. *Corrosion Science*, *33*(5), 805-814.

47 Chen, T., John, H., Xu, J., Lu, Q., Hawk, J., & Liu, X. (2013). Influence of surface modifications on pitting corrosion behavior of nickel-base alloy 718. Part 1: Effect of machine hammer peening. *Corrosion science*, *77*, 230-245.

48 Lloyd, A. C., Noël, J. J., McIntyre, S., & Shoesmith, D. W. (2004). Cr, Mo and W alloying additions in Ni and their effect on passivity. *Electrochimica Acta*, *49*(17-18), 3015-3027.

49 Biesinger, M. C., Payne, B. P., Grosvenor, A. P., Lau, L. W., Gerson, A. R., & Smart, R. S. C. (2011). Resolving surface chemical states in XPS analysis of first row transition metals, oxides and hydroxides: Cr, Mn, Fe, Co and Ni. *Applied Surface Science*, *257*(7), 2717-2730.

50 Fairley, N. (2009). *CasaXPS manual 2.3. 15. Spectroscopy*. Acolyte Science.

51 Norton, P. R., Tapping, R. L., & Goodale, J. W. (1977). A photoemission study of the interaction of Ni (100),(110) and (111) surfaces with oxygen. *Surface Science*, *65*(1), 13-36.

52 http://www.xpsfitting.com/2012/01/oxygen-1s-for-transition-metals.html. 2012

53 Maulana, RD Panji. Effect of Cathodic Protection to Hydrogen Embrittlement Susceptibility of 718 and 625Plus Nickel-Based Superalloys. MSc Thesis. University of Manchester. 2016.

54 Park, J. S., Kim, Y. S., Nam, T. H., & Kim, J. G. (2015). Effects of hydrogen charging and electro transport treatment on the anodic polarization behavior and mechanical property of Alloy 600. *Journal of the Korean Institute of Metals and Materials*, *53*(11), 770-777.

55 Boudalia, M., Guenbour, A., Bellaouchou, A., Fernandez-Domene, R. M., & Garcia-Anton, J. (2013). Corrosion behaviour of a highly alloyed austenitic alloy UB6 in contaminated phosphoric acid. *International Journal of Corrosion*, *2013*.

56 Emran, K. M., & Al-Refai, H. (2018). Resistivity and passivity characterization of Ni-base glassy alloys in NaOH media. *Metals*, *8*(1), 64.

57 Leiva-García, R., Fernandes, J. C. S., Muñoz-Portero, M. J., & Garcia-Anton, J. (2015). Study of the sensitisation process of a duplex stainless steel (UNS 1.4462) by means of confocal microscopy and localised electrochemical techniques. *Corrosion Science*, *94*, 327-341.

58 Lukacs, Z. (1997). The numerical evaluation of the distortion of EIS data due to the distribution of parameters. *Journal of Electroanalytical Chemistry*, *432*(1-2), 79-83.

59 Lukacs, Z. (1999). Evaluation of model and dispersion parameters and their effects on the formation of constant-phase elements in equivalent circuits. *Journal of Electroanalytical Chemistry*, *464*(1), 68-75.

60 Kocijan, A., Merl, D. K., & Jenko, M. (2011). The corrosion behaviour of austenitic and duplex stainless steels in artificial saliva with the addition of fluoride. *Corrosion Science*, *53*(2), 776-783.

61 Macdonald, D. D., Sun, A., Priyantha, N., & Jayaweera, P. (2004). An electrochemical impedance study of Alloy-22 in NaCl brine at elevated temperature: II. Reaction mechanism analysis. Journal of Electroanalytical Chemistry, 572(2), 421-431.

62 Macdonald, J. R., & Barsoukov, E. (2005). Chapter 4. Impedance spectroscopy: theory, experiment, and applications. *History*, *1*(8), 1-13.

63 Richard, F. Custom Age 625 Plus Alloy - A Higher Strength. Superalloys 718, 625 and Various Derivatives: Proceedings of the International Symposium on the Metallurgy and Applications of Superalloys 718, 625 and Various Derivatives. Loria, E. A. (Ed.). 1991.

64 Yu, J. G., Luo, J. L., & Norton, P. R. (2001). Effects of hydrogen on the electronic properties and stability of the passive films on iron. *Applied surface science*, *177*(1-2), 129-138

65 Yang, M. Z., Luo, J. L., Yang, Q., Qiao, L. J., Qin, Z. Q., & Norton, P. R. (1999). Effects of hydrogen on semiconductivity of passive films and corrosion behavior of 310 stainless steel.

Journal of the Electrochemical Society, *146*(6), 2107

66 Yang, Q., Qiao, L. J., Luo, J. L., & Chiovelli, S. (1999). Chemical hydrogen charging conditions for martensite transformation and surface cracking in type 304 stainless steel. *Scripta materialia*, *40*(11).

67 Guiñon Pina, V. (2011). Estidio de la Influencia de la Polarizacion anodica y catodica sobre el comportamiento electroquimico del Niquel, Cromo y Aceros Inoxidables.(Doctoral dissertation).

68 Ningshen, S., & Mudali, U. K. (2009). Hydrogen effects on pitting corrosion and semiconducting properties of nitrogen-containing type 316L stainless steel. *Electrochimica acta*, *54*(26), 6374-6382.

69 Schmuki, P., Virtanen, S., Isaacs, H. S., Ryan, M. P., Davenport, A. J., Böhm, H., & Stenberg, T. (1998). Electrochemical Behavior of Cr2 O 3/Fe2 O 3 Artificial Passive Films Studied by *In situ* XANES. *Journal of the Electrochemical Society*, *145*(3), 791.

70 Kim, H., Hara, N., & Sugimoto, K. (1999). Dependence of Corrosion Resistance of Fe2 O 3–Cr2 O 3 Artificial Passivation Films on Crystal Structure and Chemical State of Constituent Elements of the Films. *Journal of The Electrochemical Society*, *146*(10), 3679-3685.

71 Flis, J., Zakroczymski, T., Kleshnya, V., Kobiela, T., & Duś, R. (1999). Changes in hydrogen entry rate and in surface of iron during cathodic polarisation in alkaline solutions. *Electrochimica acta*, *44*(23), 3989-3997.

72 Maurice, V., Yang, W. P., & Marcus, P. (1994). XPS and STM investigation of the passive film formed on Cr (110) single-crystal surfaces. *Journal of The Electrochemical Society*, *141*(11), 3016-3027.

73 Tamm, Y et Vares, P M. (1987). Hydrogen Overvoltage on Iron in Sulphuric Acid Solutions. Elektrokhimiya, 23(9), 1269-1272.

74 Hajilou, T., Hope, M. S., Zavieh, A. H., Kheradmand, N., Johnsen, R., & Barnoush, A. (2018). In situ small-scale hydrogen embrittlement testing made easy: An electrolyte for preserving surface integrity at nano-scale during hydrogen charging. International Journal of Hydrogen Energy, 43(27), 12516-12529

75 Reartes, G. B., Morando, P. J., Blesa, M. A., Hewlett, P. B., & Matijevic, E. (1995). Reactivity of chromium oxide in aqueous solutions. 2. Acid dissolution. Langmuir, 11(6), 2277-2284.

76 Standard, A. S. T. M. (2012). F1624: Standard Test Method for Measurement of Hydrogen Embrittlement Threshold in Steel by the Incremental Step Loading Technique. *ASTM International, West Conshohocken, PA*

77 Martelo, D., Sampath, D., Monici, A., Morana, R., & Akid, R. (2019). Correlative analysis of digital imaging, acoustic emission, and fracture surface topography on hydrogen assisted cracking in Ni-alloy 625+. *Engineering Fracture Mechanics*, *221*, 106678.

78 Turnbull, A., Ballinger, R. G., Hwang, I. S., Morra, M. M., Psaila-Dombrowski, M., & Gates, R. M. (1992). Hydrogen transport in nickel-base alloys. Metallurgical Transactions A, 23(12), 3231-3244.

79 Harris, Z. D., Dolph, J. D., Pioszak, G. L., Troconis, B. C. R., Scully, J. R., & Burns, J. T. (2016). The effect of microstructural variation on the hydrogen environment-assisted cracking of Monel K-500. *Metallurgical and Materials Transactions A*, *47*(7), 3488-3510.

80 Troconis, B. R., Harris, Z. D., Ha, H., Burns, J. T., & Scully, J. R. (2017). The effect of heat-to-heat variations in metallurgy and hydrogen-metal interactions on the hydrogen embrittlement of Monel K-500. *Materials Science and Engineering: A*, *703*, 533-550.

CRediT authorship contribution statement

D.F. Martelo: Conceptualization, Methodology, Investigation, Formal analysis, Writing - Original Draft, Visualization. **Rd. Panji Maulana:** Investigation. **R. Leiva-garcia:** Conceptualization, Writing - Review & Editing. **G.R. Joshi:** Writing - Review & Editing, Methodology, Formal analysis. **R. Morana:** Project administration, Writing - Review & Editing. **R. Akid:** Conceptualization, Methodology, Project administration, Resources, Supervision, Writing - Review & Editing.

☒ The authors declare that they have no known competing financial interests or personal relationships that could have appeared to influence the work reported in this paper.

Highlights

- An interrupted H charging RSL technique was proposed to measure HE susceptibility
- The HE resistance of two nickel alloys was compared using two testing techniques
- Degradation of the passive layer after CP was observed using XPS and EIS
- No direct correlation was found between i_c, time to failure and global H content.